Mon. Not. R. Astron. Soc. **281**, 716–736 (1996)

The structure of dark matter haloes in hierarchical clustering models

Shaun Cole[1,4] and Cedric Lacey[2,3,5]

[1]*Department of Physics, University of Durham, Science Laboratories, South Rd, Durham DH1 3LE*
[2]*Physics Department, University of Oxford, Keble Rd, Oxford OX1 3RH*
[3]*Theoretical Astrophysics Center, Blegdamsvej 17, DK-2100 Copenhagen O, Denmark*
[4]*Shaun.Cole@durham.ac.uk*
[5]*lacey@tac.dk*

Accepted 1996 March 5. Received 1996 February 12; in original form 1995 October 30

ABSTRACT

We use a set of large cosmological N-body simulations to study the internal structure of dark matter haloes which form in scale-free hierarchical clustering models (initial power spectra $P(k) \propto k^n$ with $n = 0, -1$ and -2) in an $\Omega = 1$ universe. We find that the radius r_{178} in a halo corresponding to a mean interior overdensity of 178 accurately delineates the quasi-static halo interior from the surrounding infalling material, in agreement with the simple spherical collapse model. The interior velocity dispersion correlates with mass, again in good agreement with the spherical collapse model. Interior to the virial radius r_{178}, the spherically averaged density, circular velocity and velocity dispersion profiles are well fitted by a simple two-parameter analytical model proposed by Navarro, Frenk & White. This model has $\rho \propto r^{-1}$ at small radii, steepening to $\rho \propto r^{-3}$ at large radii, and fits our haloes to the resolution limit of the simulations. The two model parameters, scalelength and mass, are tightly correlated. Lower mass haloes are more centrally concentrated, and so have scalelengths which are a smaller fraction of their virial radius than those of their higher mass counterparts. This reflects the earlier formation times of low-mass haloes. The haloes are moderately aspherical, with typical axial ratios 1 : 0.8 : 0.65 at their virial radii, becoming gradually more spherical towards their centres. The haloes are generically triaxial, but with a slight preference for prolate over oblate configurations, at least for $n = -1$ and 0. These shapes are maintained by an anisotropic velocity dispersion tensor. The median value of the spin parameter is $\lambda \approx 0.04$, with a weak trend for lower λ at higher halo mass. We also investigate how the halo properties depend on the algorithm used to identify them in the simulations, using both friends-of-friends and spherical overdensity methods. We find that, for groups selected at mean overdensities $\sim 100 - 400$ by either method, the properties are insensitive to how the haloes are selected, if the halo centre is taken as the position of the most bound particle.

Key words: cosmology: theory – dark matter.

1 INTRODUCTION

The structure of dark matter haloes is of fundamental importance to understanding the formation and evolution of galaxies and galaxy clusters. In hierarchical clustering models, galaxies form by gas cooling and condensing in dark matter haloes, and clusters form by the gravitational aggregation of individual galaxies and galaxy groups. This evolution is driven by gravitational instability via accretion and merging. Many studies have been made of the properties of haloes formed by dissipationless gravitational collapse using N-body simulations, which are ideally suited to investigate this inherently non-linear problem. Continuing advances in computer technology and codes have enabled ever larger simulations to be performed, allowing halo structure to be examined in ever increasing detail.

Pioneering N-body studies of the structure of haloes formed by hierarchical clustering in an expanding universe were carried out by Frenk et al. (1985) and Quinn, Salmon & Zurek (1986). These concentrated on halo density profiles, and found approximately flat rotation curves for $\Omega = 1$ cold dark matter (CDM) models, corresponding to density varying with radius roughly as $\rho \propto r^{-2}$. Frenk et al. (1988) made a detailed study of haloes in CDM models in flat, open and closed universes, using a P^3M code with 32^3 particles, calculating rotation curves, shapes and angular momenta of haloes. Efstathiou et al. (1988) made a similar study of haloes in self-similar clustering models with $\Omega = 1$ and scale-free initial conditions,

meaning initial power spectra of the form $P(k) \propto k^n$, with $n = 1, 0, -1$ and -2. These studies, and those of Quinn et al. (1986) and Zurek, Quinn & Salmon (1988), which used a combination of PM and PP methods and comparable numbers of particles, found that the slopes of halo density profiles varied both with spectral index n and with Ω.

More recently, there have been studies with higher resolution and/or more particles. Warren et al. (1992) simulated $\Omega = 1$ scale-free models using a tree-code and $\sim 10^6$ particles. They concentrated on the radial variation of shapes and the distribution of angular momentum in their better-resolved haloes. Crone, Evrard & Richstone (1994) used 64^3-particle P^{3}M simulations to study the density profiles of haloes in a variety of cosmological models for scale-free initial conditions. They fitted these density profiles to power laws. However, they only examined the most massive haloes in each simulation. Navarro, Frenk & White (1996) used a hierarchical tree-code to simulate the formation of a small number of haloes of very different masses in the CDM model at high resolution, again to study the density profiles. Dubinski & Carlberg (1991) also simulated individual haloes at high resolution, but with a much cruder treatment of the tidal effects of material outside the halo.

In this paper, we analyse the structure of haloes formed in self-similar clustering models, with $\Omega = 1$ and spectral indices $n = -2, -1, 0$. Scale-free initial conditions are conceptually simple, and, over limited mass ranges, provide useful approximations to physical models (such as CDM) whose power spectra have a slope which varies slowly with mass. For example, in the standard CDM model, the effective slope is $n \approx -2$ on the scale of galaxy haloes ($M \sim 10^{12}\,\mathrm{M}_\odot$) and $n \approx -1$ on the scale of galaxy clusters ($M \sim 10^{15}\,\mathrm{M}_\odot$). Such models also have the great advantage that their self-similar scaling properties can be used to distinguish physical effects from artifical features introduced by the limitations of the numerical simulations. Our simulations use the P^{3}M code of Efstathiou et al. (1985), with $128^3 \approx 2 \times 10^6$ particles. Unlike Warren et al. (1992), we employ periodic boundary conditions. As in the previous studies, we pay particular attention to halo density profiles and rotation curves, but we also study the radial variation of other dynamical properties, the departures from spherical symmetry and the dependence of these properties on initial conditions. We also investigate how these properties depend on halo mass.

We are interested in haloes as objects in approximate dynamical (or virial) equilibrium. An important issue not addressed in detail in previous studies is where one should draw the boundary of the virialized region of the halo, and what group-finding method works best for partitioning a simulation into virialized objects. Previous studies have each just used a single method of identifying the haloes (although several methods have been tried), and presented results for that one method, without investigating how the halo properties might depend on the method used. In the present paper, we consider several possible criteria for deciding where the boundary of the virialized region is. We also compare results obtained using two different group-finding methods, friends-of-friends (Davis et al. 1985) and the spherical overdensity method of Lacey & Cole (1994), for a range of overdensities.

The plan of the paper is as follows. In Section 2 we define virial mass and length scales for haloes, and compare three analytical halo models which we later use to fit our numerical results. Section 3 describes the N-body simulations, and how we identify the groups within them and construct radial profiles of halo properties. In Section 4, we examine the scalings of bulk properties of the haloes with mass, and make a critical comparison of the different group-finding algorithms. In Section 5, we examine in detail the spherically averaged halo profiles, which we compare with the analytical models of Section 2. Section 6 discusses the angular momenta of haloes. Departures from spherical symmetry are investigated in Section 7. Our understanding of these results and their implications are discussed in Section 8, and we conclude in Section 9.

2 HALO MODELS

The analytical model most often used to describe the formation of dark matter haloes is the idealized collapse of a uniform, spherically symmetric overdense region. For $\Omega = 1$, collapse to a singularity occurs when linear theory would predict an overdensity of $\delta_c = 3/20(12\pi)^{2/3} \approx 1.69$. If one argues that realistic amounts of substructure present before the collapse will lead to violent relaxation, then the virial theorem and energy conservation imply that after virialization the object will have a density of $18\pi^2 \approx 178$ times the background density $\bar{\rho}$, if the final equilibrium state is also a uniform sphere. Real dark matter haloes are not uniform spheres, but we will refer to the radius r_{178} around the halo centre within which the mean density is $178\bar{\rho}$ as the 'virial radius'. This terminology will be justified by the results presented in Section 5, where we will see that the radius r_{178} approximately demarcates the inner regions of haloes at $r \lesssim r_{178}$ which are in approximate dynamical equlibrium from the outer regions at $r \gtrsim r_{178}$ which are still infalling. The corresponding 'virial mass' and circular velocity are given by

$$M_{178} = \frac{4\pi}{3}\, 178\, \bar{\rho}\, r_{178}^3, \tag{2.1}$$

and

$$V_{178} = \left(\frac{GM_{178}}{r_{178}}\right)^{1/2}. \tag{2.2}$$

These quantities prove to be useful for characterizing the global properties of realistic dark matter haloes.

Below we describe three equilibrium models for the internal structure and kinematics of DM haloes, which we will later compare with the properties of the haloes formed in a set of large cosmological N-body simulations. These models are the singular isothermal sphere, the Hernquist (1990) and the Navarro, Frenk & White (1995) (hereafter NFW) models. The latter two models differ from the isothermal sphere in having shallower density gradients in the inner parts and steeper gradients in the outer parts. All three models are intended to represent only the regions interior to the virial radius r_{178}. The Hernquist model has finite total mass, while isothermal sphere and NFW models both have infinite total mass. The Hernquist and NFW models can both be considered, in some sense, as only minor modifications of the isothermal sphere, as, interior to the virial radius, the density ρ is approximately proportional to r^{-2} over the region containing most of the mass. The density, circular velocity and velocity dispersion profiles of these models are compared in Fig. 1 for particular values of the scale parameters.

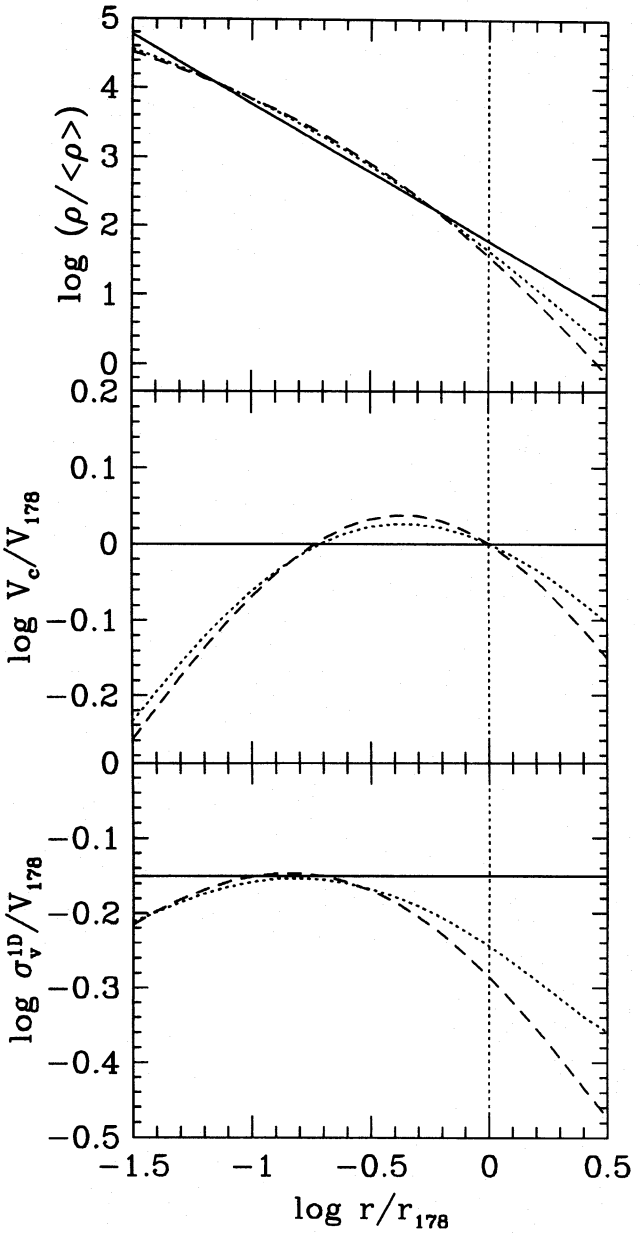

Figure 1. Comparison of the density, ρ, circular velocity, V_c, and velocity dispersion, σ_v^{1D}, profiles for the singular isothermal sphere (solid) and the isotropic Hernquist (dashed) and NFW (dotted) models. In the NFW model the parameter $a_N = 0.2$, as advocated to model the density profile of a CDM galaxy cluster by Navarro et al. (1995), and $a_H = 0.43$ in the Hernquist model so that both have circular velocity profiles that peak at $r \approx 0.43 r_{178}$. The 'virial radius' r_{178} is marked by the vertical dotted line.

2.1 The singular isothermal sphere

A standard model for dark matter haloes, motivated by flat rotation curves, is the singular isothermal sphere, for which the density profile is

$$\rho(r) \propto \frac{1}{r^2}. \tag{2.3}$$

Defining $s \equiv r/r_{178}$ as the radial distance in units of the virial radius, we can rewrite this as

$$\frac{\rho(s)}{\bar{\rho}} = \frac{178}{3}\frac{1}{s^2}. \tag{2.4}$$

The corresponding expression for the mass within radius r, scaled to the value at the virial radius, is

$$\frac{M(s)}{M_{178}} = s. \tag{2.5}$$

The circular velocity is constant with radius,

$$\frac{V_c(s)}{V_{178}} = 1, \tag{2.6}$$

and, assuming dynamical equilibrium and an isotropic velocity distribution, the one-dimensional velocity dispersion is also constant,

$$\frac{\sigma_v^{1D}(s)}{V_{178}} = \sqrt{2}. \tag{2.7}$$

In their relatively low-resolution CDM simulations, Frenk et al. (1985, 1988) and Quinn et al. (1986) found halo circular velocities which were essentially constant with radius down to the gravitational softening radius, consistent with this simple model. This model, truncated at the virial radius, has been widely used as a description of the dark matter haloes formed in hierarchical clustering models, e.g. in the modelling of gravitational lensing statistics by Narayan & White (1988), and in the galaxy formation models of Kauffmann, White & Guiderdoni (1993) and Cole et al. (1994).

2.2 The Hernquist model

Hernquist (1990) presented a completely analytical model which closely approximates the de Vaucouleurs $R^{1/4}$ law that has long been used to fit the surface brightness profiles of elliptical galaxies. The density profile has the form

$$\rho(r) \propto \frac{1}{r(r+b_H)^3}. \tag{2.8}$$

Defining a dimensionless radius $s \equiv r/r_{178}$ as before, and a dimensionless scale radius $a_H \equiv b_H/r_{178}$, the density, mass, potential ψ and circular velocity can be written in dimensionless form as

$$\frac{\rho(s)}{\bar{\rho}} = 178\frac{2}{3}\frac{a_H(1+a_H)^2}{s(s+a_H)^3}, \tag{2.9}$$

$$\frac{M(s)}{M_{178}} = \frac{(1+a_H)^2 s^2}{(s+a_H)^2}, \tag{2.10}$$

$$\frac{\psi(s)}{V_{178}^2} = -\frac{(1+a_H)^2}{(s+a_H)}, \tag{2.11}$$

$$\frac{V_c(s)}{V_{178}} = \frac{(1+a_H)}{(s+a_H)}s^{1/2}. \tag{2.12}$$

The parameter a_H sets the scale at which the slope of the density profiles changes from r^{-1} at small r, to r^{-4} at large r. The circular velocity profile peaks at $r = a_H r_{178}$ (see Fig. 1). The main attraction of this model is that it has an analytical distribution function which can be expressed in terms of elementary functions. It has also been used by Dubinski & Carlberg (1991) to fit the density profiles of galactic haloes formed in their N-body simulations.

Assuming dynamical equlibrium, the radial velocity dispersion, $\sigma_r(r)$, of the model can be obtained by integrating the Jeans equation

$$\frac{1}{\rho}\frac{\mathrm{d}}{\mathrm{d}r}(\rho\sigma_r^2(r)) + 2\beta\frac{\sigma_r^2(r)}{r} = -\frac{\mathrm{d}\psi}{\mathrm{d}r}, \tag{2.13}$$

where $\beta \equiv 1 - \sigma_\theta^2(r)/\sigma_r^2(r)$. For the case of isotropic orbits, the radial and tangential velocity dispersions are equal, $\sigma_\theta(r) = \sigma_r(r)$. For this case Hernquist (1990) finds

$$\frac{\sigma_r^2(s)}{V_{178}^2} = \frac{(1+a_H)^2}{(12a_H)}\left\{\frac{12s(s+a_H)^3}{a_H^4}\ln\left(\frac{s+a_H}{s}\right) - \frac{s}{s+a_H}\left[25 + 52\left(\frac{s}{a_H}\right) + 42\left(\frac{s}{a_H}\right)^2 + 12\left(\frac{s}{a_H}\right)^3\right]\right\}. \tag{2.14}$$

2.3 The NFW model

Navarro et al. (1995) proposed an alternative analytical density profile, which they found to be an excellent fit to the dark matter haloes of galaxy clusters formed in their CDM simulations. Navarro et al. (1996) found this profile to apply over a large range of masses from those of dwarf galaxies to galaxy clusters. The density profile has the form

$$\rho(r) \propto \frac{1}{r(r+b_N)^2}. \tag{2.15}$$

Defining $a_N \equiv b_N/r_{178}$, the density, mass, potential and circular velocity can be written as

$$\frac{\rho(s)}{\bar{\rho}} = \frac{178}{3}\frac{f(a_N)}{s(s+a_N)^2}, \tag{2.16}$$

$$\frac{M(s)}{M_{178}} = f(a_N)\left[\ln\left(1+\frac{s}{a_N}\right) - \frac{s}{(s+a_N)}\right], \tag{2.17}$$

$$\frac{\psi(s)}{V_{178}^2} = -f(a_N)\frac{\ln(1+s/a_N)}{s}, \tag{2.18}$$

$$\frac{V_c(s)}{V_{178}} = \frac{f(a_N)^{1/2}}{s^{1/2}}\left[\ln\left(1+\frac{s}{a_N}\right) - \frac{s}{(s+a_N)}\right]^{1/2}, \tag{2.19}$$

where, for compactness, we have defined

$$f(a_N) = \frac{1}{\left(\ln\left(1+1/a_N\right) - 1/(1+a_N)\right)}. \tag{2.20}$$

Like the Hernquist profile, $\rho \propto r^{-1}$ as $r \to 0$, but the asymptote at large r is now r^{-3} rather than r^{-4}, which leads to a logarithmically divergent total mass. The parameter a_N, again, defines the scale of the transition between the inner and outer slopes, which occurs more gradually in this model than in the Hernquist model (see Fig. 1). The slope of the density profile is $\mathrm{d}\ln\rho/\mathrm{d}\ln r = -2$ at $r = a_N r_{178}$. The circular velocity peaks at $r = 2.16a_N r_{178}$. Also shown in Fig. 1 is the one-dimensional velocity dispersion, σ_v^{1D}, obtained by numerically integrating equation (2.13), again assuming isotropic orbits and dynamical equilibrium.

3 SIMULATIONS AND GROUPS

3.1 Simulations

The simulations we have analysed are the three scale-free simulations which were used to study the statistics of mergers in an $\Omega = 1$ universe by Lacey & Cole (1994). The simulations were performed using the high-resolution particle-particle-particle-mesh (P^3M) code of Efstathiou et al. (1985) with $128^3 \approx 2 \times 10^6$ particles. The long-range force was computed on a 256^3 mesh, while the softening parameter for the short-range force was chosen to be $\eta = 0.2(L/256)$, where L is the size of the (periodic) computational box. The corresponding potential can be approximated by a Plummer law with softening $\epsilon \approx \eta/3 = L/3840$. The initial power spectra of the simulations were power laws, $P(k) \propto k^n$, with $n = -2$, -1 and 0. More details are given in Lacey & Cole (1994).

In this paper we analyse almost exclusively the last output from each of the three simulations. At this output the three simulations have expanded by a factor 27.8, 13.3 and 6.3 and the characteristic mass is $M_* = 266$, 447 and 46.8 particles for $n = 0$, -1 and -2 respectively. Here we define the characteristic mass, M_*, such that the rms linear density fluctuation in spheres containing mass M_* is 1.69 – this being the linear theory density corresponding to the collapse to a singularity of a uniform spherically symmetric perturbation. To test for the effects of resolution we occasionally analyse a set of earlier outputs from these simulations at which the values of M_* were a factor of 4 smaller.

3.2 Group finders

We wish to study the intrinsic properties of non-linear self-bound structures that form via gravitational instability in the N-body simulations. For this reason we have identified these structures using different group-finding algorithms to ensure that the properties we quantify are intrinsic to the structures and not artefacts of any particular group-finding algorithm. Thus to identify the groups in the N-body simulation we employed two different group-finding algorithms, the standard friends-of-friends (hereafter FOF) algorithm of Davis et al. (1985) and the spherical overdensity (hereafter SO) algorithm described in Lacey & Cole (1994).

FOF groups are constructed by linking together all pairs of particles whose separation is less than b times the mean inter-particle separation. This results in groups bounded by a surface of approximately constant density, $\rho/\bar{\rho} \approx 3/(2\pi b^3)$. This elegantly simple algorithm has been used extensively in previous analyses of N-body simulations, usually with $b = 0.2$ (e.g. Frenk et al. 1988; Efstathiou et al. 1988). It succeeds in picking out most of the groups one can identify by eye, but occasionally can join together two or more distinct density centres that are linked by a tenuous bridge of particles. We will denote groups defined using this algorithm by FOF(b) .

The SO algorithm first ranks all the particles in the simulation by their local density, computed from the distance to their 10th nearest neighbour. Then, starting with the densest, a sphere is grown around this centre until the enclosed density drops below some threshold, $\kappa\bar{\rho}$. The group centre is redefined to be the centre of mass of the selected region and the process of growing the sphere and selecting a new region repeated iteratively until the group centre and group membership converge. Particles assigned to a group in this way are removed from the density-ranked list and not considered further. Then in the same manner each of the remaining ungrouped particles in the ranked list is used as a group centre. Finally, small groups inside or overlapping with larger groups are merged into the larger object. This algorithm selects spherical regions whose

average density is equal to $\kappa\bar{\rho}$. A similar method, with a mean overdensity of 180, has been used by Warren et al. (1992). We denote groups found in this way by SO(κ).

3.3 Halo profiles

In constructing halo profiles we have chosen to include all the particles surrounding the group and not only those assigned to the group by the group-finding algorithm. In each of the groups defined above we locate the particle with the most negative gravitational potential energy. The potential is calculated using only the group particles, and assuming that the potential due to each particle is $-1/(r^2+\epsilon^2)^{1/2}$, with $\epsilon = \eta/3$. We then use this as the centre of the group and inflate a sphere around this centre until the enclosed density drops below $178\bar{\rho}$. The radius of this sphere and the mass it encloses define r_{178} and M_{178} for the group. We use r_{178}, M_{178} and the corresponding V_{178} to scale the halo profiles. These choices allow a fair comparison of groups of different masses and groups located using different algorithms. The question of which algorithm best divides the simulation into discrete virialized groups then becomes largely a matter of which returns a group mass close to the virialized mass, which we will see is close to our adopted definition of the virial mass M_{178}. The relation between M_{178} and the original group mass, $M_{\rm group}$, is studied in Section 4.

For each group centre we estimate a comprehensive selection of the properties of the surrounding material binned both in spherical shells and cumulatively within spheres. These properties include: the density, circular velocity, radial velocity, radial and tangential velocity dispersions, rotation velocity, angular momentum, axial ratios of the moment of inertia tensor and virial ratio. All internal velocities are computed relative to the centre of mass velocity of the sphere of radius r_{178}. The radial bins are chosen to be equally spaced for the innermost 10 bins and then with logarithmically increasing widths out to an outer radius of $10r_{178}$. The spacing of the inner bins is chosen such that the innermost bin, which in general is the least populated, typically contained 10 particles. When computing profiles averaged over all haloes within a mass range, the bin radii were scaled with r_{178}. We examine individual profiles constructed in this way, and also mean profiles of the scaled quantities ($\rho/\bar{\rho}$, $V_{\rm c}/V_{178}$ etc.) averaged over groups within mass bins. The mass bins were chosen to cover a factor 2 in mass. With the exception of the density profile, the mean profiles evaluated in spherical shells are weighted means. We gave equal weight to all shells in the individual profiles that contained 10 or more particles and zero weight to those containing fewer than 10 particles. This procedure was adopted to avoid low particle numbers producing a large scatter in profiles such as the velocity dispersion as a function of radius. For each of the mean profiles we also accumulated the group-to-group dispersion at each radius. These dispersions can be used to place errorbars on each of the profiles which reflect the group-to-group variation.

Table 1 gives the distribution of masses in each of the three simulations for centres identified by SO(178). The large numbers of groups enable the mean profiles in each mass range to be determined very precisely. This then enables the dependence of halo profiles on mass and spectral index to be examined in some detail, but care must be taken to assess how resolution, which in terms of r_{178} worsens with decreasing M_{178}/M_*, affects these profiles. It is for this reason that we will also examine the profiles of groups extracted from an earlier output of the simulations when M_* was a factor 4 smaller.

Table 1. The distribution of SO(178) groups by mass in the three simulations. The last line gives the mass M_* in terms of the number of particles.

Spectral Index M_{178}/M_*	$n=0$	$n=-1$	$n=-2$
32–64	–	–	16
16–32	–	–	72
8–16	1	14	134
4–8	29	42	310
2–4	222	141	649
1–2	692	282	1280
0.5–1	1563	592	2486
0.25–0.5	2832	1109	4786
M_*	266	447	46.8

4 BULK PROPERTIES

We first look at the basic global properties of individual groups selected using the various group finders. As we will see in Section 5, when we study the dynamical structure of the haloes, the radius r_{178} corresponds well with the boundary at which there is a transition from general infall to approximate dynamical equilibrium. Thus the virial mass of the halo is well approximated by M_{178}. It is therefore interesting to see how the group mass defined by the various algorithms compares with M_{178}, as this acts as a measure of how well the particular group finders succeed in partitioning the simulation into discrete virialized systems. We see in Fig. 2 that for each group definition the group mass, $M_{\rm group}$, correlates strongly with M_{178}, but the offset of the correlation and the scatter around it vary. The offset between $M_{\rm group}$ and M_{178} is easily understood. Groups found using high κ or small b are typically denser and less massive than those found using small κ or large b, and so they are the central regions or sub-clumps of the less dense groups. Note that for FOF the offset is smallest for FOF(0.2). The scatter in each relation is of more interest. As is to be expected from the similarity of their definitions, the scatter between $M_{\rm group}$ and M_{178} is smallest for SO(178) groups. In this case, the essential difference in the definitions of $M_{\rm group}$ and M_{178} is the choice of group centre. For SO(178) the group is centred by its centre of mass, while M_{178} is evaluated around the centre defined by the particle in the SO(178) group with the most negative gravitational potential energy, where the potential energy is evaluated using only the group particles. This difference is generally not significant as can be seen by the fact that many of the points fall exactly on the line $M_{\rm group} = M_{178}$. For SO groups identified with other values of the density contrast, κ, the scatter grows. For the dense SO(400) groups there is a tail of objects with $M_{178} \gg M_{\rm group}$, for which the SO(400) group is simply the core of a larger virialized halo. For FOF(0.2) or (0.3) the scatter about the mean correlation is asymmetric with a tail of haloes with $M_{\rm group} > M_{178}$. As the linking length b is increased this tail becomes more pronounced, extending to $M_{\rm group} > 2M_{178}$. These outliers arise

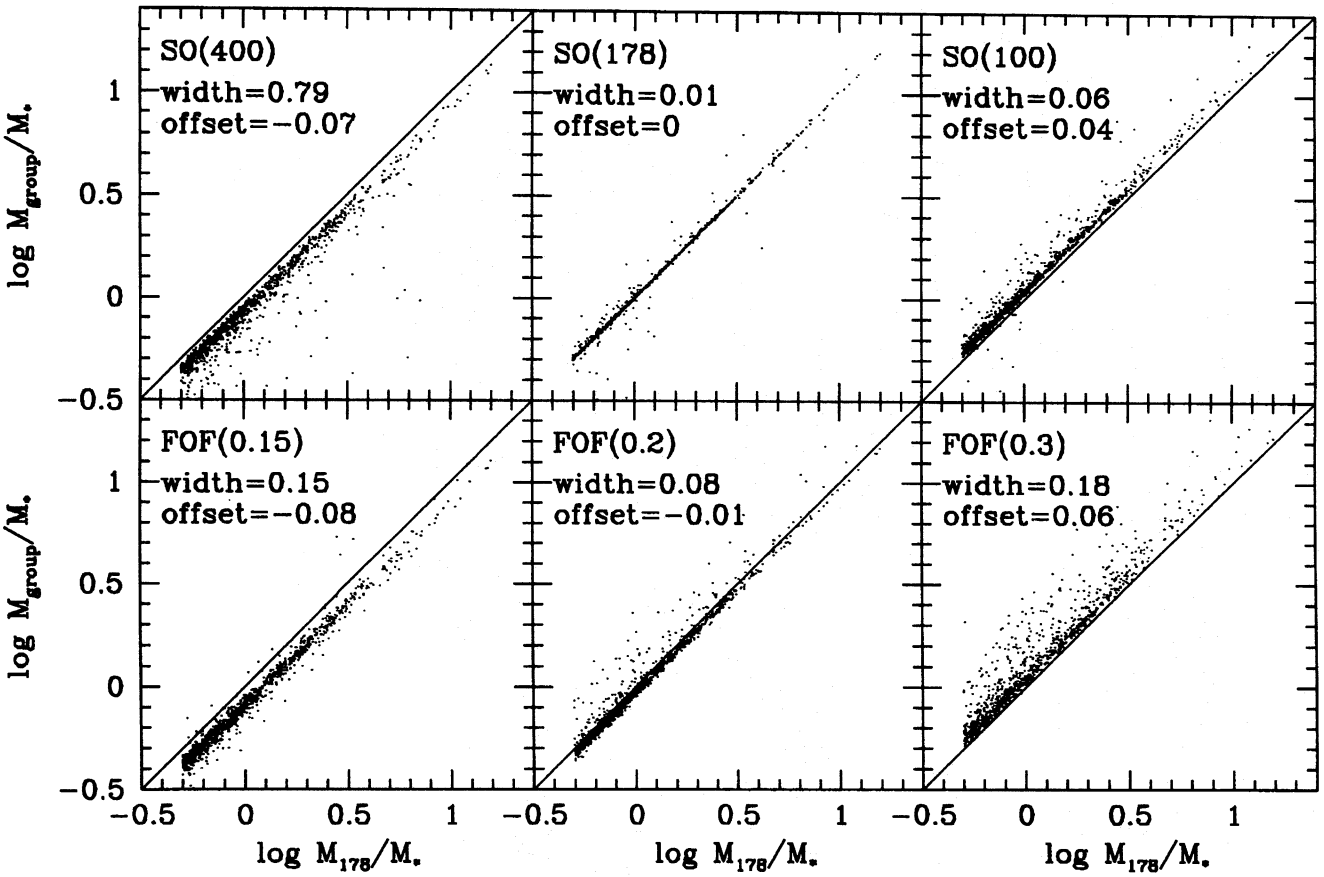

Figure 2. Scatter plots of $M_{\rm group}$ versus M_{178} for groups identified in the $n = -1$ simulation using each of the group finders SO(400), SO(178), SO(100), FOF(0.15), FOF(0.2) and FOF(0.3). The mass M_* equals 447 particles for this simulation. The straight line indicates the locus $M_{\rm group} = M_{178}$. This line is omitted from the SO(178) plot where it would obscure most of the data points. The offset given in each panel is the median of $\log_{10}(M_{\rm group}/M_{178})$. Also specified is the width of the distribution in $\log_{10}(M_{\rm group}/M_{178})$ measured between the 10th and 90th percentiles.

when two or more distinct density centres become linked by tenuous bridges of particles.

Fig. 3 shows the correlation of the one-dimensional velocity dispersion averaged within r_{178} with the mass M_{178}. The correlation agrees well with the expectation of the isothermal sphere model (Section 2.1), $\sigma_{\rm v}^{\rm 1D} = V_{178}/\sqrt{2} \propto M_{178}^{1/3}$, with an rms scatter about this mean relation of only 10–15 per cent. For the groups selected at high density contrast, particularly SO(400), a tail of groups appears with $\sigma_{\rm v}^{\rm 1D} > V_{178}/\sqrt{2}$. In these cases, it seems likely that the sphere of radius r_{178} is actually only part of a significantly larger virialized structure.

Groups selected at low density contrast, particularly those located by FOF, tend to be composites of distinct virialized structures, while, on the other hand, groups identified at higher density contrast are often only small clumps within larger structures. Overall the FOF(0.2) and SO(178) group masses and M_{178} correlate well. Thus both group-finding algorithms are good candidates for selecting virialized structures. The disadvantage of the SO(178) algorithm is that it forces spherical boundaries on the groups when we shall see that groups are typically triaxial in shape. The FOF(0.2) algorithm does not force any particular geometry on groups, but because it is only sensitive to the local density it is prone to occasional merging of separate virialized systems that are linked by tenuous bridges.

5 SPHERICALLY AVERAGED PROFILES

We now examine the spherically averaged radial profiles of haloes and compare them with the analytical models described in Section 2.

5.1 Massive haloes

Figs 4, 5 and 6 show various mean profiles (averaged over mass bins) around the centres of the massive SO(178) and FOF(0.2) groups from each of the three simulations. Here, and in all subsequent plots of radial profiles, two dotted vertical lines mark the force-softening scale η and virial radius r_{178}. Note that the effective softening for the P^{3}M code is often taken be $\epsilon = \eta/3$. The upper two panels show the mean circular velocity, $V_{\rm c} \equiv (GM(< r)/r)^{1/2}$, and density profiles. The density profiles flatten and the circular velocities turn up at large radii, $r \gg r_{178}$, where material not physically bound or associated with the group becomes included in the profile. Thus the density tends to the mean density at large r and the circular velocity becomes proportional to radius. Also shown on these figures are the corresponding Hernquist and NFW profiles which have been fitted to the SO(178) mean density profile over the range $\eta < r < r_{178}$. The fits were performed by converting the group-to-group dispersion of the density

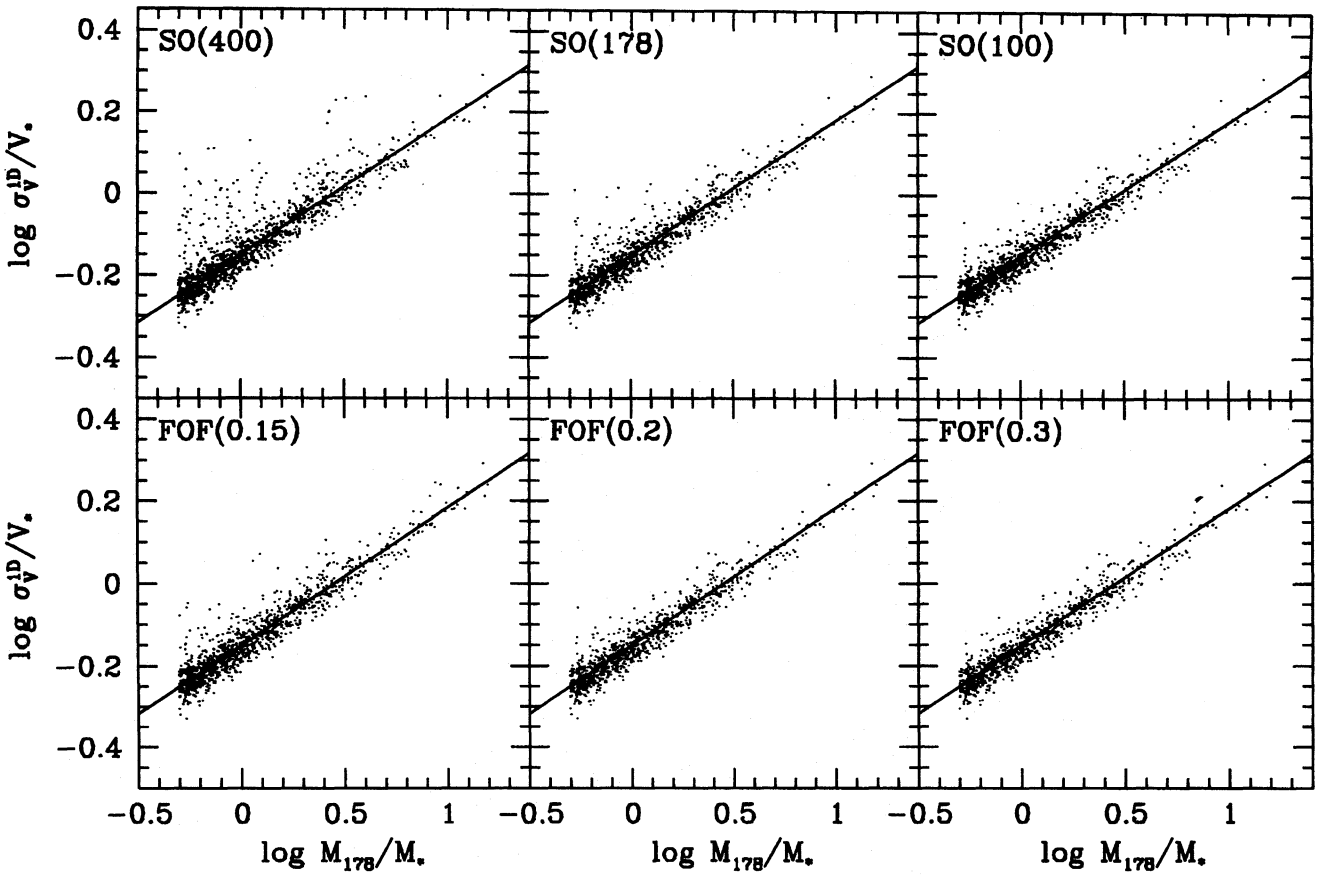

Figure 3. Scatter plots of mean one-dimensional velocity dispersion, σ_v^{1D}, within the virial radius, r_{178}, versus the mass M_{178} for groups identified in the $n = -1$ simulation using each of the group finders SO(400), SO(178), SO(100), FOF(0.15), FOF(0.2) and FOF(0.3). The mass M_* equals 447 particles for this simulation. V_* is V_{178} for a halo with $M_{178} = M_*$. The straight line indicates the locus $\sigma_v^{1D} = V_{178}/2^{1/2}$, which is the prediction of the isothermal sphere model.

profiles at each radius into an effective error on the mean profile. The scale parameters a_H and a_N of the Hernquist and NFW models were then varied to achieve minimum-χ^2 fits. Visually, both models are excellent fits to the halo density profiles between the virial radius, r_{178}, and the force-softening scale η, for each value of n. The NFW model in particular continues to be a good match to the halo profiles at larger radii, where we will see that the halo is not yet in equilibrium, and at smaller radii where resolution is likely to have affected the halo structure. A more telling comparison is that between the model and N-body circular velocity profiles. Note that by definition these are all constrained to pass through the same point at r_{178}. We see that the Hernquist model changes slope too abruptly to match that of the haloes. The NFW profile is a significantly better match.

The lower panels of Figs 4, 5 and 6 show various mean kinematic properties of the haloes. These are the rotation speed V_{rot} in spherical shells around the axis defined by the angular momentum vector of the shell, the mean radial velocity V_r, radial velocity dispersion $\sigma_r = \langle (V_r - \langle V_r \rangle)^2 \rangle^{1/2}$, and velocity dispersion anisotropy $\sigma_\theta(r)/\sigma_r(r)$, where $\sigma_\theta^2 = \langle V_\theta^2 \rangle$ is the tangential velocity dispersion. In each case the velocities are defined with respect to the centre of mass motion of all the material interior to radius r_{178}. To a first approximation the rotation velocity is small and the velocity dispersion isotropic and almost independent of radius, all in agreement with the simple isotropic isothermal sphere model. A more detailed inspection shows that $V_{rot}/\sigma_r \approx 0.3$, which, although appreciable, implies that the rotation is not a significant contributor to the dynamical support of the halo. Interior to r_{178}, σ_θ/σ_r is slightly less than unity, indicating a tendency for radial orbits, particularly at $r \approx r_{178}$. Outside the virial radius σ_θ/σ_r increases and slightly overshoots unity before settling to the isotropic value, $\sigma_\theta/\sigma_r = 1$, at large radii. Overlying the velocity dispersion profiles are the model predictions of the fitted Hernquist and NFW models, computed assuming spherical symmetry and $\sigma_\theta/\sigma_r = 1$ ($\beta = 0$), from the Jeans equation (2.13). We see that, within the virial radius, both match well the slow curvature in the corresponding halo σ_r profile.

The lowest curve in the lower panels of Figs 4, 5 and 6 is the mean radial velocity, V_r, of material in shells. These curves are the main evidence we have that the radius r_{178} is an accurate characterization of the virial radius of the haloes. In each case V_r is approximately zero interior to r_{178}, consistent with a dynamically relaxed system. Between r_{178} and $4r_{178}$ $V_r < 0$, indicating material in the process of falling on to the central halo. At larger radii, V_r begins to increase, passing through $V_r = 0$ at the turn-around radius and matching on to the general Hubble flow at large r. The location of the turn-around radius is in good agreement with the spherical

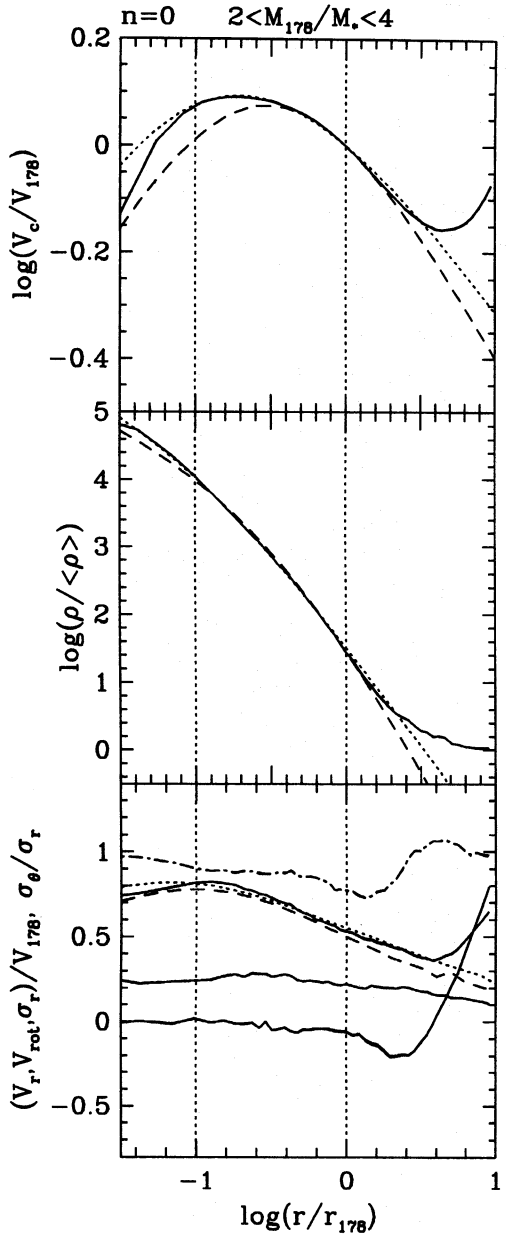

Figure 4. The solid curves in the upper and middle panels show mean circular velocity and mean density profiles of all groups with $2 < M_{178}/M_\bullet < 4$ ($532 < N < 1064$) in the $n = 0$ simulation located by both SO(178) and FOF(0.2). In this case the lists of group centres defined by SO(178) and FOF(0.2) were identical. The smooth curves in these two panels are the Hernquist (dashed) and NFW (dotted) models which have been fitted to the density profiles over the range between the vertical dotted lines which mark the force-softening scale η and virial radius r_{178}. The lower panel shows a variety of measures of the dynamical state of the haloes. The lowest solid curve is the mean radial velocity, V_r, as a function of radius. The next solid curve is the mean rotation speed, V_{rot}. The upper dot-dashed curve is σ_θ/σ_r, which measures the anisotropy of the velocity dispersion. The remaining solid curve traces the mean radial velocity dispersion as a function of radius. The smooth dashed and dotted curves are respectively the Hernquist and NFW models for the velocity dispersion assuming isotropy, $\sigma_\theta/\sigma_r = 1$.

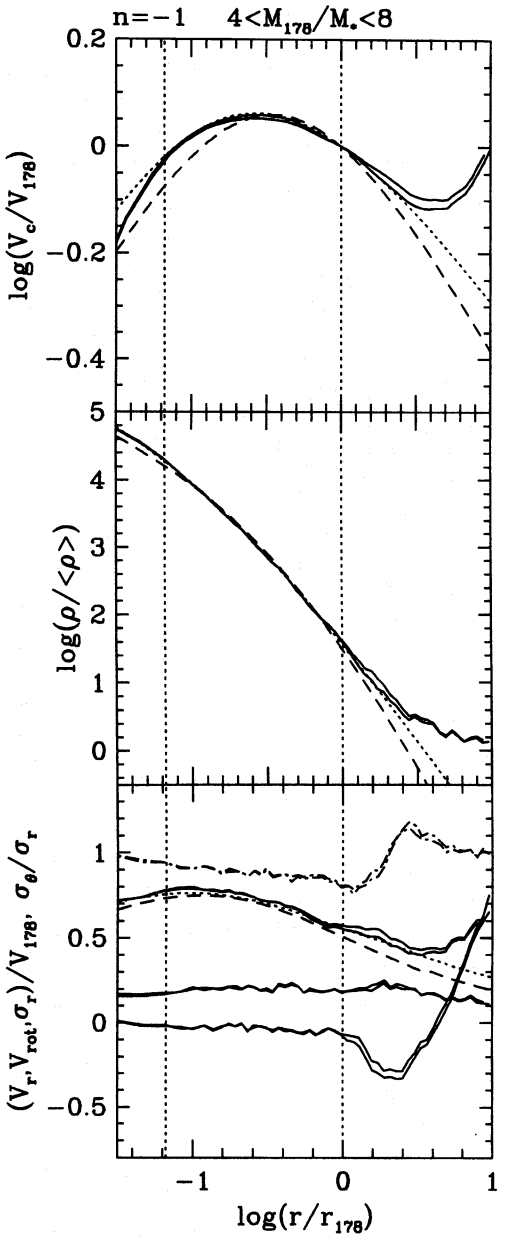

Figure 5. As Fig. 4, but for groups from the $n = -1$ simulation with masses in the range $4 < M_{178}/M_\bullet < 8$ ($1788 < N < 3576$). Here the lists of group centres produced by the SO(178) and FOF(0.2) algorithms were slightly different and thus two slightly different curves are visible for each profile.

collapse model which predicts a mean density interior to the turn-around radius of $(3\pi/4)^2 \approx 5.55$. Similar results for the radial velocity were found by Crone et al. (1994).

The typical group-to-group variation of the radial velocity pattern and the corresponding density profiles is illustrated in Fig. 7, which shows the profiles for five groups taken from the $n = -1$ simulation with masses in the range $8 < M_{178}/M_\bullet < 16$. Although the profiles can be significantly perturbed by substructure in the individual haloes, the transition from infall to quasi-static equilibrium at $r \approx r_{178}$ is quite clear in the majority of cases. However, the radial velocity profiles are too noisy to make them useful for determining the boundary of the virialized region for individual haloes.

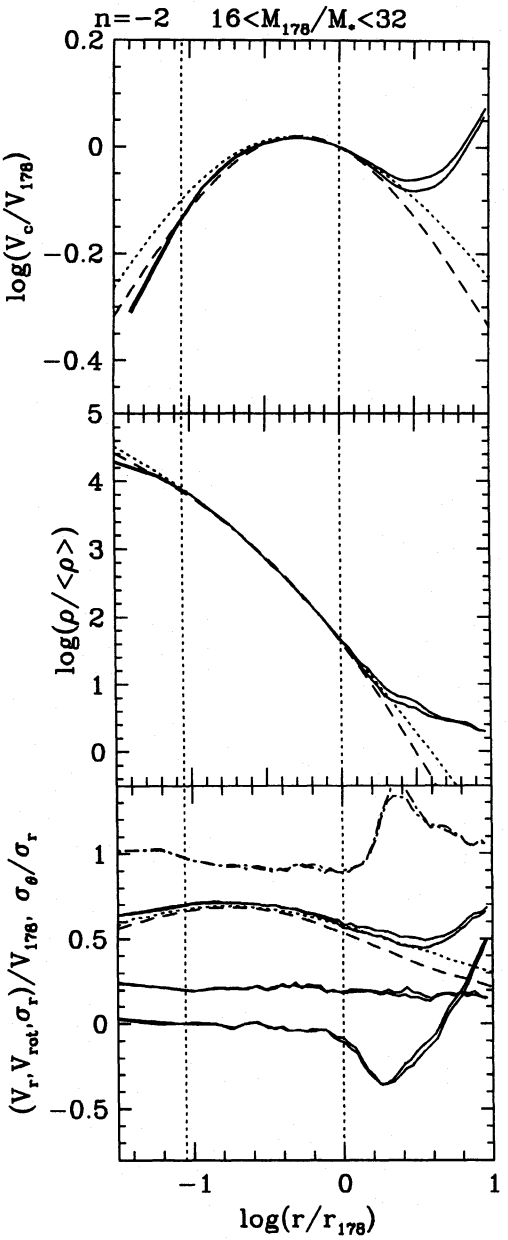

Figure 6. As Fig. 5, but for groups from the $n = -2$ simulation with masses in the range $16 < M_{178}/M_* < 32$ ($749 < N < 1498$).

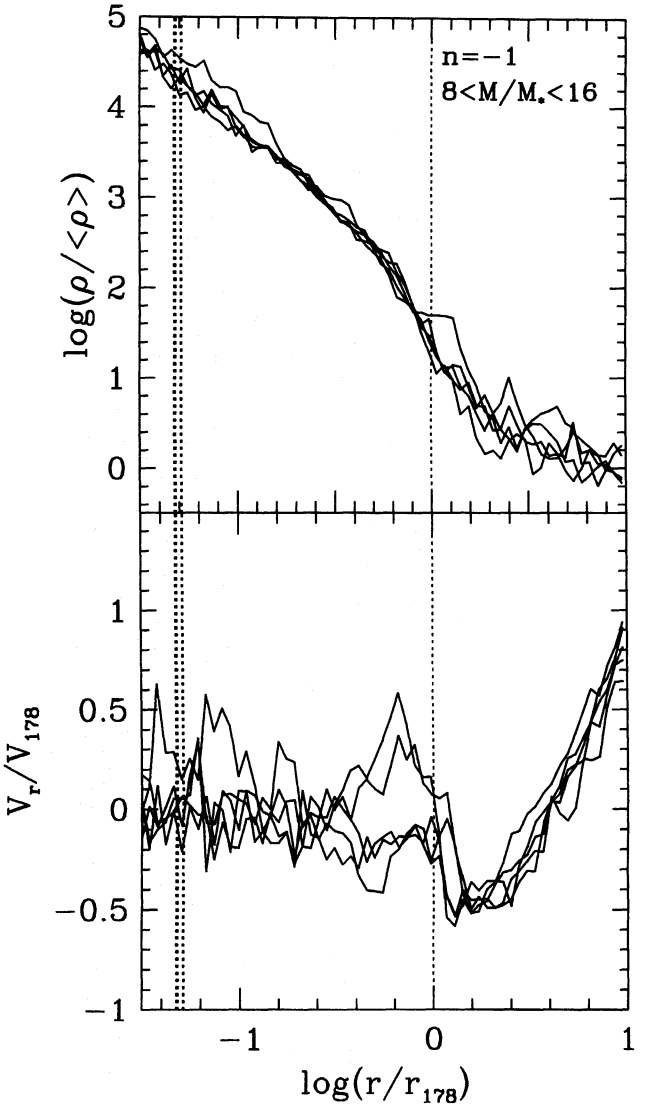

Figure 7. The density and radial velocity profiles of a selection of five groups taken from the $n = -1$ simulation with masses in the range $8 < M_{178}/M_* < 16$ ($3576 < N < 7152$).

Another measure of dynamical equilibrium within haloes is provided by the virial ratio $2T/|W|$. The expectation for an isolated system in dynamical equilibrium is for the total binding energy to equal twice the total kinetic energy, $2T = |W|$. As an example, Fig. 8 plots the mean value of the virial ratio $2T/|W|$ evaluated within spheres for groups from the $n = -1$ simulation with masses in the range $8 < M_{178}/M_* < 16$. Here T is the kinetic energy of the material within a sphere of radius r and W the self-gravitational binding energy of the same material, i.e. neglecting the the effect on the gravitational potential of all material at larger radii. The ratio $2T/|W|$ should approach unity at the boundary of the virialized region if surface terms in the virial theorem vanish. We find $2T/|W|$ approaches unity only slowly at large radii and is significantly greater than unity at $r = r_{178}$. However this same profile is tracked quite well by the same quantity evaluated from the fitted analytical Hernquist and NFW models, which when integrated over all the mass accurately obey the virial theorem. Thus, although the haloes are believed to be in reasonably good dynamical equilibrium within $r < r_{178}$, the ratio $2T/|W|$ is not useful for defining the boundary of the virialized region.

5.2 Mass-dependent trends

In the previous section we saw that the NFW model provides an excellent description of the spherically averaged structure of the more massive haloes formed in each of the three simulations. We now turn to how the halo structure depends on mass. The density and circular velocity profiles for a range of masses in each of the three simulations are shown in Figs 9 and 10. Also shown are Hernquist and NFW models which have been fitted to the density profiles over the range $\eta < r < r_{178}$. Over this range, the NFW model is an excellent description

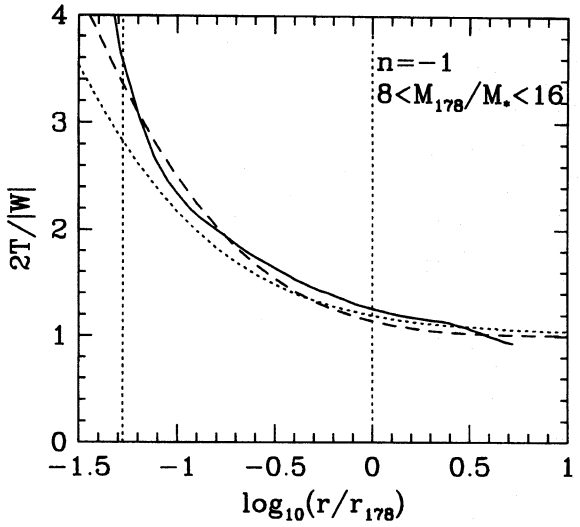

Figure 8. The solid curve shows the mean virial ratio, $2T/|W|$, evaluated within spheres, as a function of radius, for haloes with masses in the range $8 < M_{178}/M_* < 16$ ($3576 < N < 7152$) from the $n = -1$ simulation. The dashed and dotted curves show respectively the corresponding profiles for the Hernquist and NFW models that were fitted to the mean density profiles of these groups.

of the halo density profiles for almost the full range of masses investigated in each of the simulations. Very close to the softening radius η the density profiles of the most massive haloes are slightly steeper than those of the NFW model. For lower masses the fitted NFW models also match the inner portion of the halo density profiles at $r < \eta$, in all cases except the low-mass groups of the $n = -2$ simulation. Although not apparent to the eye, the Hernquist models are formally worse fits to the halo density profiles than the NFW models. They tend to be marginally too steep in the outer parts of the haloes and too shallow in the inner regions. Nevertheless they are a considerable improvement over a simple isothermal model, which has $\rho \propto r^{-2}$ at all radii.

The differences between the NFW and Hernquist models are more pronounced in plots of the circular velocity profiles, Fig. 10. Here we again see that the NFW models match well the profiles of the haloes over the entire region of the fit. In contrast the Hernquist models peak too sharply and underestimate the circular velocity in the central regions of the haloes.

We now turn to the question of systematic variations of the halo density profiles with mass, M_{178}/M_*. Here we have to be very careful to distinguish between real physical effects and the consequences of the limited resolution of the N-body simulations. If the finite number of particles or the force resolution were artificially suppressing the density in the centre of the simulated haloes then we would expect the radius of the affected region to be directly proportional to η. In contrast we see in Fig. 10 that the peak in the circular velocity profiles moves to smaller r/r_{178} for lower mass haloes while at the same time η/r_{178}, marked by the inner vertical line, increases. This is the first piece of evidence that gives us confidence that the form of the density and circular velocity profiles is not predominately due to limited resolution. A more stringent test comes from analysing the haloes with the same values of M_{178}/M_*, but extracted from an earlier output of each simulation when M_* was smaller by a factor 4, and therefore η/r_{178} larger by a factor 1.59. An example of this comparison is shown in Fig. 11 which compares the mean density profiles of groups in the $n = -1$ simulation at the two output times. We note that the two density profiles agree quite accurately for radii greater than η, the force-softening scale of the less well-resolved output. Fig. 12 shows the dependence of the scale parameters a_N and a_H on M_{178}/M_* for each of the three simulations and for the two output times. The fits were made to the binned mean density profiles over the range $\eta < r < r_{178}$ using estimates of the error on the mean profile obtained from the group-to-group variance about the mean divided by the number of groups. Standard χ^2-fits were made, treating each data point as independent and formal 1σ errors on the fit parameters estimated from the points adjacent to the best fit where $\Delta\chi^2 = 1$. The error bars on Fig. 12 show the $\pm 5\sigma$ bounds. If numerical resolution were the sole reason for the existence of the detectable break in the halo density profiles, then we would expect the scalelengths a_N or a_H to scale as $M^{-1/3}$ at a given output time, and we would expect the values from the earlier output to be 60 per cent larger than those from the final output. In fact they are typically less than 20 per cent larger than their better resolved counterparts from the final output of each simulation. Thus, although the measured scalelengths must have some residual dependence on the numerical resolution, the detected trends with mass and spectral index are real. The scalelengths, a_N or a_H, increase with increasing mass M_{178}/M_*, and the steepness of this relation depends on the spectral index n.

We also examined the mean profiles of velocity dispersion, anisotropy, rotation velocity and radial velocity for haloes in all mass ranges. The results, shown in Fig. 13, are very similar for the different masses. In particular, the radial velocity always starts to go significantly negative (indicating the edge of the virialized region) at $r \approx r_{178}$.

The distribution with mass of the ratio $(2T/|W|)_{178}$, evaluated in spheres of radius r_{178}, is shown in Fig. 14, for the $n = -1$ simulation. There is no tendency for the lower mass, less well-resolved haloes to be further from virial equilibrium than the larger mass haloes. In fact, the median value of $(2T/|W|)_{178}$ is 1.1 at low masses and increases gradually to approximately 1.2 at $M_{178}/M_* = 10$. This trend is completely consistent with the variation of the halo density profiles reported above. The ratio $2T/|W|$ at the virial radius can be computed for the NFW model. For $a_N = 0.1$, which fits the density profiles of haloes of mass $M_{178} \approx M_*$, $(2T/|W|)_{178} = 1.13$, while for $a_N = 0.2$, which corresponds to $M_{178} \approx 10M_*$, $(2T/|W|)_{178} = 1.23$. At all masses there is a tail of objects with larger values of $(2T/|W|)_{178}$. These are probably examples of ongoing mergers such as depicted in Fig. 17(c) later.

6 ANGULAR MOMENTUM

The dimensionless spin parameter

$$\lambda = \frac{J|E|^{1/2}}{GM^{5/2}}, \tag{6.1}$$

where J, E and M are the total angular momentum, energy and mass, is an important dynamical parameter that has been much studied in numerical simulations (e.g. Barnes & Efstathiou

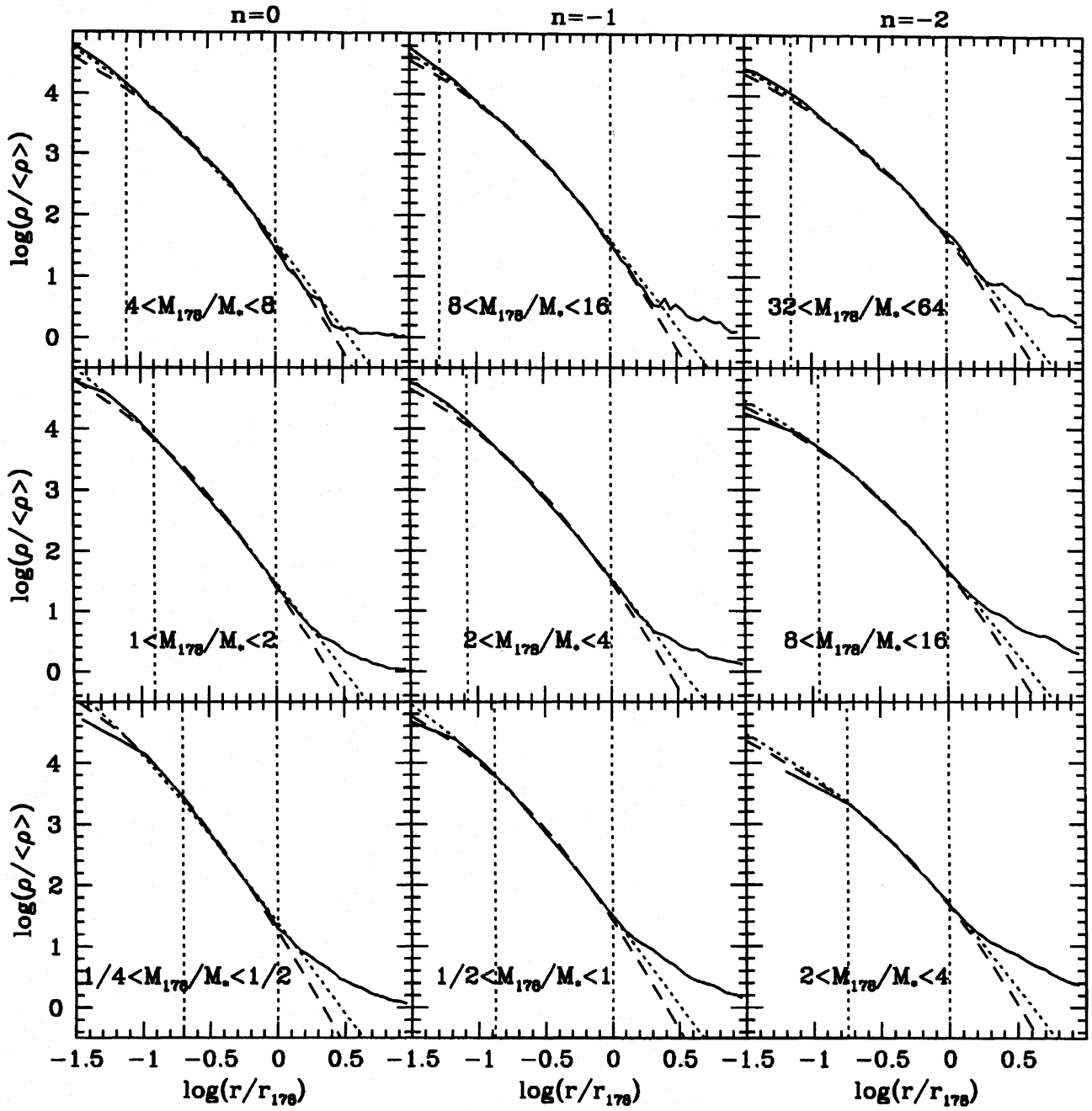

Figure 9. The mean density profiles of SO(178) groups of a variety of masses from each of the three self-similar simulations. The two dotted vertical lines mark the force-softening scale, η, and virial radius, r_{178}. The smooth curves are NFW (dotted) and Hernquist (dashed) model fits to the profiles in the range $\eta < r < r_{178}$. Note that M_* equals 266, 447 and 46.8 in the $n = 0$, -1 and -2 simulations respectively.

1987). Our results are in broad agreement with earlier work and have a median $\lambda \approx 0.04$ at $M = M_*$. Fig. 15 shows, as a function of mass, the distributions of λ_{178} evaluated for spheres of radius r_{178}. The median, 20th and 80th percentiles are indicated by the solid lines. They reveal no obvious variation in the distributions with spectral index, but a weak trend towards decreasing values of λ_{178} with increasing mass. The earlier outputs from the simulations confirm that this trend is real, and not simply a result of the effective numerical resolution varying with mass. The overall distributions and trends with mass are in good agreement with those of Barnes & Efstathiou (1987), who studied the distribution of λ for CDM and $n = 0$ models, and those reported by Efstathiou et al. (1988), who investigated other scale-free models. Efstathiou et al. also found a weak dependence of the median value of λ on spectral index, but for a fixed M_{178}/M_* we find any such dependence to be extremely weak. For example, for $1/2 < M_{178}/M_* < 2$, we find median values for λ_{178} of 0.045, 0.043 and 0.044 for $n = 0$, -1 and -2 respectively, with uncertainties of about 0.001. For $2 < M_{178}/M_* < 4$, we find medians of 0.034, 0.037 and 0.038 with uncertainties of around 0.002. Efstathiou et al. may have found a stronger trend because,

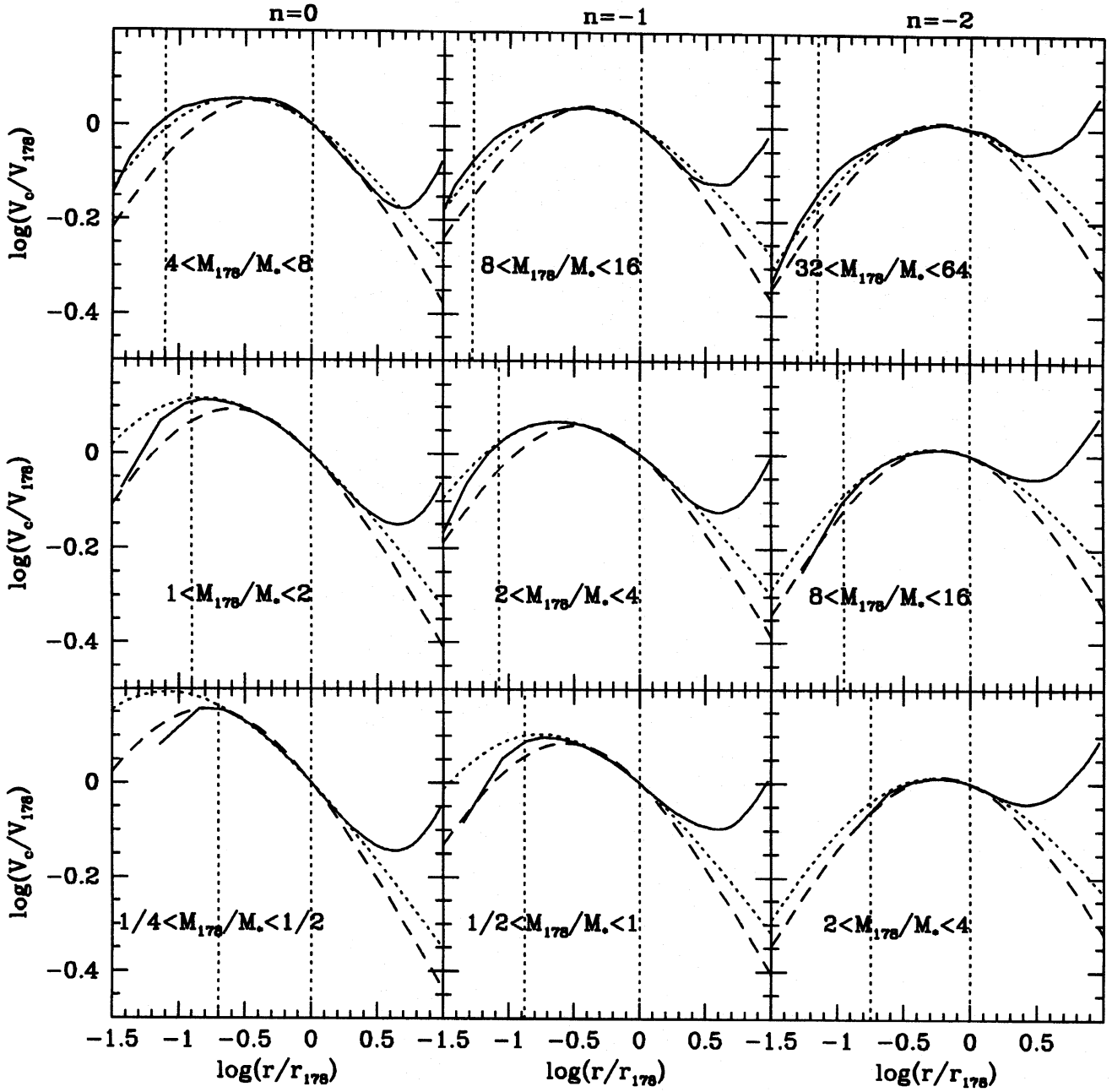

Figure 10. This figure shows the circular velocity profiles and model fits corresponding to Fig. 9.

by averaging over all the haloes in each simulation, they gave different weights to different ranges of $M/M_\bullet$ for different n.

The degree of alignment of the angular momentum throughout each halo is studied in Fig. 16. For each halo we measured the angle θ_J between the angular momentum vector of material in shells or spheres of radius r and the total angular momentum vector of the material within the virial radius r_{178}. As a function of radius, Fig. 16 shows the mean value of $\cos(\theta_J)$ for shells (solid curves) and spheres (dashed curves) for haloes selected in various mass ranges from each of the three simulations. If the angular momentum were randomly orientated then $\langle\cos(\theta_J)\rangle = 0$. We find some degree of alignment through the virialized region of the haloes, with a sharp drop in the alignment beyond r_{178}. The estimate of the degree of alignment is sensitive to the noise in estimates of J. Thus, the true alignment may be somewhat better than indicated by this analysis. A more detailed study of the angular momentum distribution can be found in Warren et al. (1992).

7 ASYMMETRY AND SUBSTRUCTURE

In the previous analysis, by spherically averaging we have treated the haloes as if they were both smooth and intrinsically spherical. In reality, the haloes are non-spherical and contain significant substructure. Figs 17(a)–(d) show examples of four groups selected from the $n = -1$ simulation to illustrate the variety of morphologies. Each group is shown projected along

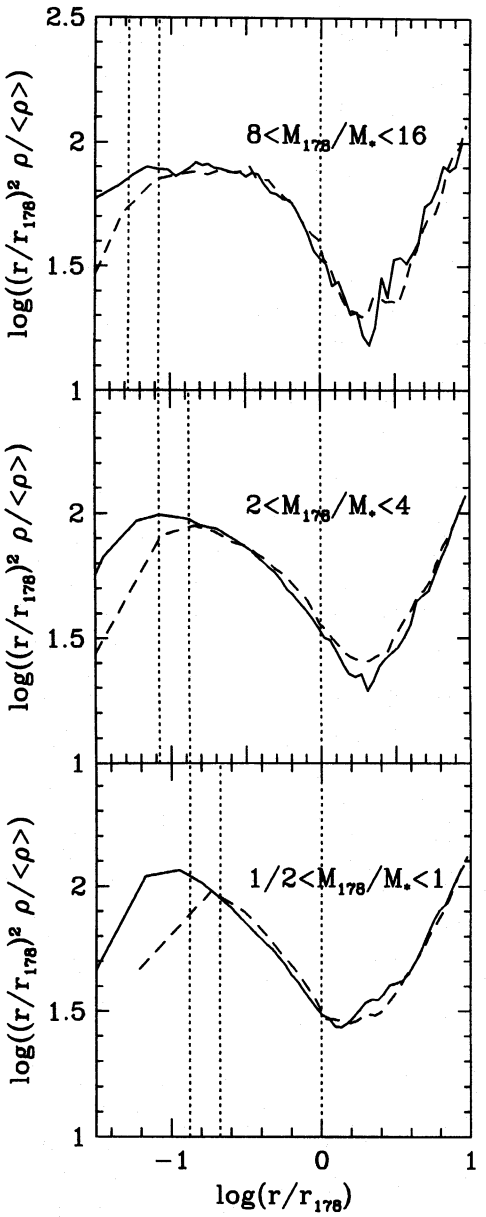

Figure 11. A comparison of the mean density profiles of SO(178) groups of a variety of masses in the $n = -1$ simulation at two different output times. The solid curves are the mean density profiles from the final output, and are the same as those plotted in the central column of Fig. 9 except here we plot $\log((r/r_{178})^2\rho/\langle\rho\rangle)$ so as to expand the vertical scale. The dashed curves are the corresponding profiles from an earlier output in which the groups are less well resolved. At this earlier time $M_* = 112$ particles, a factor 4 less than at the final time. The inner two vertical dotted lines mark the force-softening scale η in the two cases. The outer dotted line marks the virial radius r_{178}.

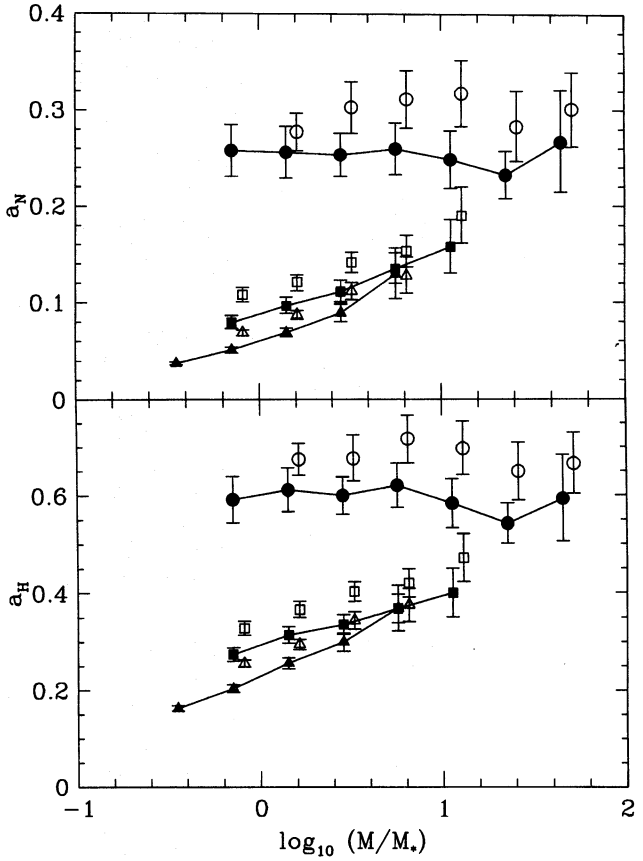

Figure 12. The variation of the scale parameters a_N and a_H of the NFW and Hernquist model fits to the halo density profiles. The solid symbols are the parameter values from the fits to the mean density profiles of the groups from the final output of each simulation. The circles, squares and triangles are for $n = -2, -1$ and 0 respectively. M_* for these outputs corresponds to 266, 477 and 46.8 particles. The open symbols, plotted displaced slightly to the right, are the corresponding parameter values obtained from earlier simulation outputs when the characteristic masses, M_*, were a factor 4 smaller. The error bars on each point indicate the $\pm 5\sigma$ range, where the formal 1σ errors were obtained from the $\Delta\chi^2 = 1$ points of the χ^2-fits to the mean density profiles.

each of the three principal axes of the inertia tensor of the material within the radius r_{178}, whose orientation is indicated by the dotted ellipse in each panel. The particles plotted are those identified as group members by the SO(178) algorithm. The contours show the projected surface density of all particles within $2r_{178}$ of the group centre. For these groups the outermost contours agree extremely well with the projected boundaries of the same groups when identified using the FOF(0.2) algorithm.

The first two groups, Figs 17(a)–(b), are typical of the majority of groups. There is a good correspondence between the FOF(0.2) and SO(178) group definitions and both have centres of mass that coincide quite well with the potential centre. The offset between these two centres is indicated in the upper panel of each figure. The remaining two groups are examples where the FOF(0.2) algorithm links together two distinct haloes which are in the process of merging. In such cases the offset between the potential centre and group centre of mass can be large for the FOF(0.2) group, but remains small for the SO(178) definition. Thus, for the FOF(0.2) groups, there is a correlation between the morphology and the offset between the centre of mass and the potential centre. Approximately 20 per cent of FOF(0.2) groups have $d_{off} > 0.3r_{178}$.

To quantify the distribution of halo shapes and their radial dependence within individual groups, we have studied the first and second moments of the mass distribution within spheres.

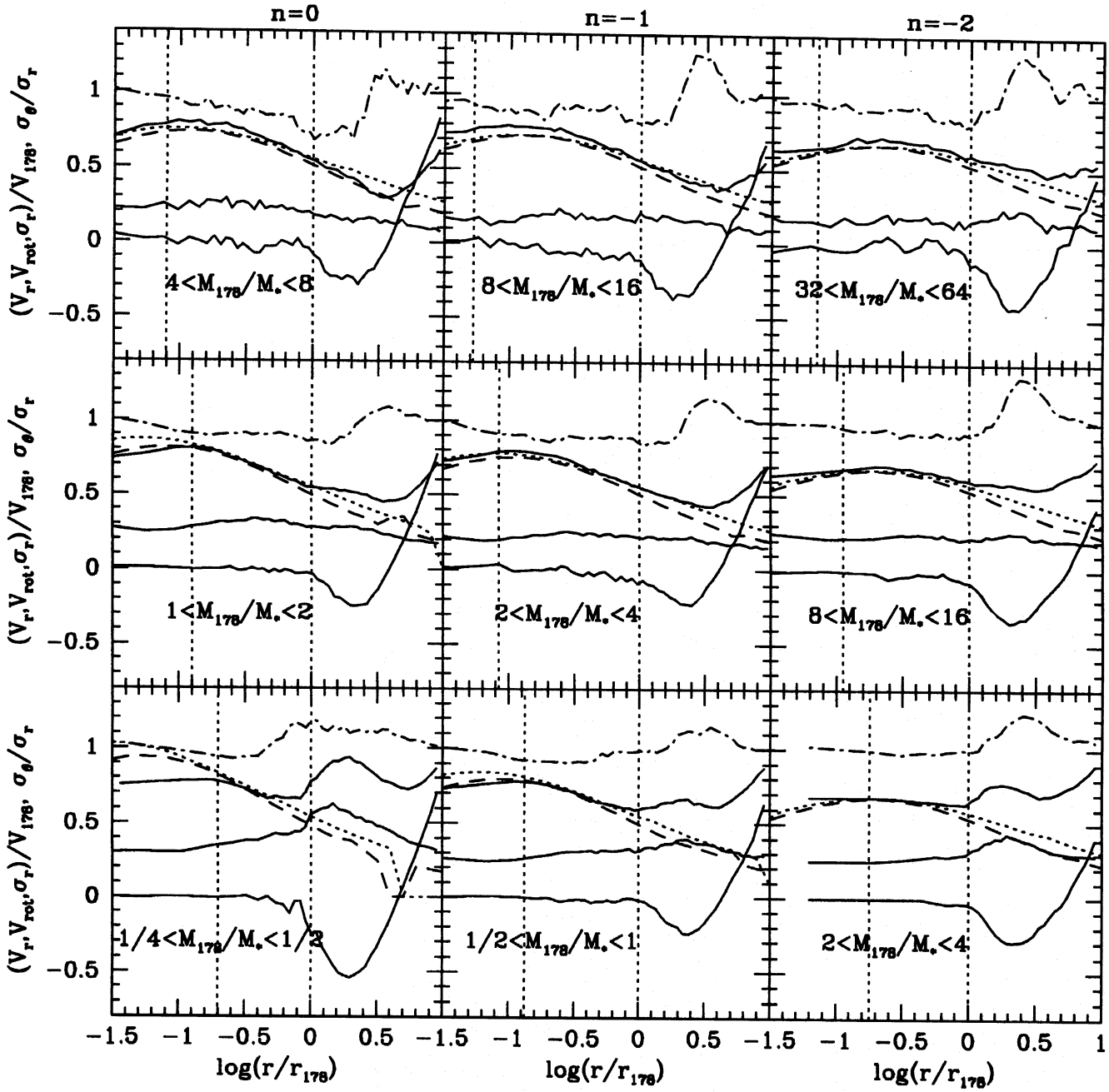

Figure 13. This figure shows the mean profiles of kinematical properties corresponding to Fig. 9. The lowest solid curve in each panel is the measured radial velocity V_r, followed by rotation speed V_{rot} and radial velocity dispersion σ_r, and the upper dot-dashed curve is the velocity dispersion anisotropy. The smooth dashed and dotted curves are the predictions of the isotropic Hernquist and NFW models respectively, based on the fits to the density profiles shown in Fig. 9.

The first moments define a dipole vector, whose first component is

$$L_x(r) = \sum_{\text{sphere}} x/N_{\text{sphere}}, \tag{7.1}$$

where the summation is over all N_{sphere} particles interior to radius r. The statistic that we study is a normalized magnitude of this vector, $D(r) = |L(r)|/\langle r\rangle_r$, where $\langle r\rangle_r$ is the mass-weighted mean value of r within the sphere. This definition implies that an isotropic distribution has $D(r) = 0$, while the maximum value of $D(r)$ is unity corresponding to all the mass concentrated in one direction.

The second moments of the mass distribution define the components of the inertia tensor. For example

$$I_{xy}(r) = \sum_{\text{sphere}} xy/N_{\text{sphere}}, \tag{7.2}$$

where the summation is again over all particles interior to radius r. If we denote the ordered eigenvalues of this tensor as a^2, b^2 and c^2, then the mass distribution can be characterized by an ellipsoid with axial ratios $a : b : c$. We study these

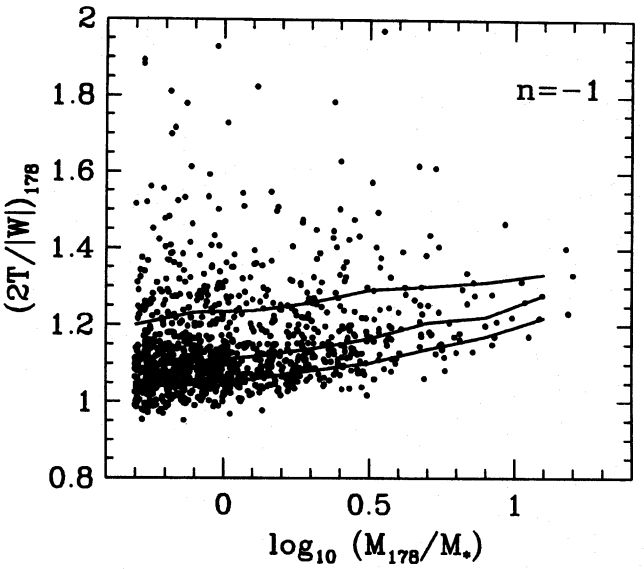

Figure 14. The scatter in the virial ratio evaluated interior to r_{178} versus mass for the $n = -1$ simulation. The curves mark the loci of the 20th, 50th and 80th percentiles of the distribution. The mass M_* equals 447 particles.

axial ratios as a function of radius r, and also a normalized quadrupole statistic which may be written in terms of these eigenvalues as

$$Q(r) = \frac{\left(2(a^2+b^2+c^2)^2 - 6(a^2b^2+b^2c^2+c^2a^2)\right)^{1/2}}{\langle r^2\rangle_r}, \qquad (7.3)$$

where $\langle r^2\rangle_r$ is the mass-weighted mean value of r^2 within the sphere. An isotropic distribution has $Q(r) = 0$ while the maximum value is $Q(r) = \sqrt{2}$.

Fig. 18 shows the mean axial ratios and quadrupole and dipole statistics for a selection of well-resolved haloes from each simulation. For fixed M_{178}/M_* poorly resolved haloes from the earlier output time of our simulations have noisier and larger quadrupoles. For all mass ranges the halo shapes become increasingly aspherical – small values of b/a and c/a and large values of $Q(r)$ and $D(r)$ – at radii smaller than the force-softening scale η. At larger radii, for haloes containing more than approximately 100 particles within r_{178}, we find that these profiles have very little systematic dependence on mass. One can also see from Fig. 18 that the profiles also have negligible dependence on the spectral slope of the initial conditions. The typical mean axial ratios $a : b : c$ are $1 : 0.8 : 0.65$ at the virial radius r_{178}. The axial ratio profiles indicate that the haloes gradually become more spherical with decreasing radius until one approaches the force-softening scale. The dipole and quadrupole statistics are slowly increasing throughout the range $\eta < r < r_{178}$, with typical values of 0.15 and 0.25 at the virial radius. Beyond the virial radius, the random distribution of the material falling towards the halo results in a sharp decline in the axial ratios b/a and c/a and a corresponding sharp increase in both $D(r)$ and $Q(r)$.

The distribution of axial ratios $a : b : c$ at the virial radius is shown in Fig. 19. This figure combines all haloes with masses $M_{178} > M_*$, but splitting the samples reveals no significant mass dependence. For each spectral index the

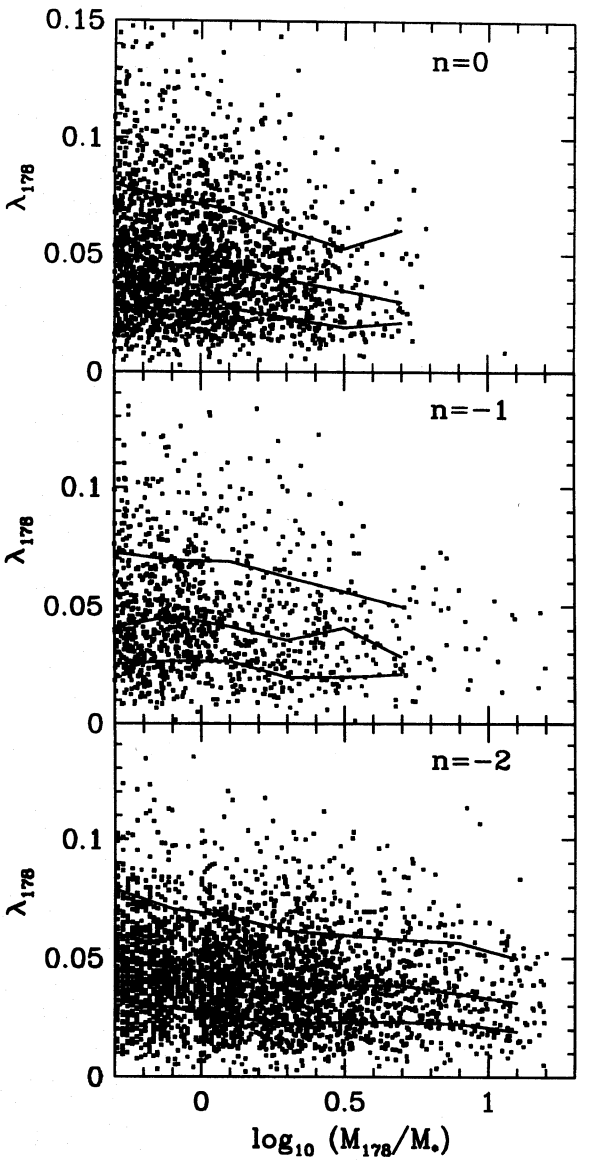

Figure 15. The distribution of the spin parameter λ_{178}, evaluated for material within a sphere of radius r_{178}, against mass. The lines mark the loci of the 20th, 50th and 80th percentiles of the distribution. Note that M_* equals 266, 447 and 46.8 in the $n = 0$, -1 and -2 simulations respectively.

distribution of axial ratios is broad, with all haloes being to some degree triaxial. For spectral indices $n = -1$ and 0 prolate configurations ($c/b < b/a$) are mildly favoured over oblate ($c/b > b/a$), but no such trend is evident in the case of $n = -2$.

Our conclusions about axial ratios are in general agreement with those of Efstathiou et al. (1988). Our values for the typical axial ratios also agree with Warren et al. (1992), when for the latter we compare with the values they calculate from the inertia tensor within spheres. Warren et al. also use a method of fitting ellipsoids to the density distribution, from which they find a trend for haloes to become more spherical with increasing radius, opposite to the trend we find.

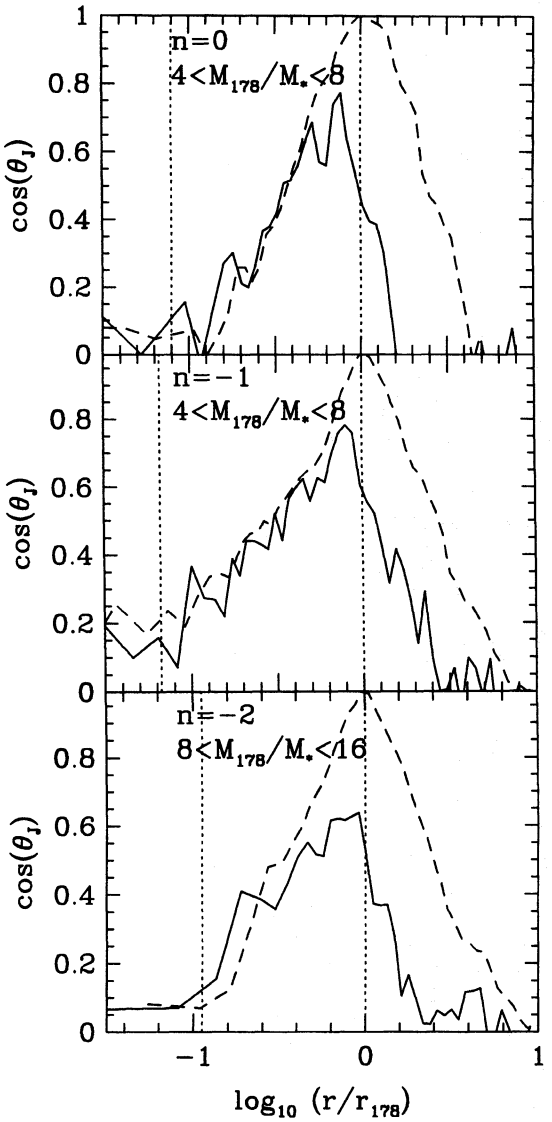

Figure 16. The alignment of the angular momentum within haloes. The angle θ_J is the angle between the total halo angular momentum, computed from all the material interior to the virial radius r_{178}, and the angular momentum of material in shells or spheres. The curves give the mean value of $\cos(\theta_J)$ for shells (solid curves) and spheres (dashed curves) where the averaging is done over all the haloes in the specified mass ranges.

8 DISCUSSION

To the limit of the resolution of our simulations, the densities of dark matter haloes diverge as one approaches their centres. As a first approximation, the density profiles between the gravitational-softening scale and the virial radius are fitted by power laws, in agreement with Crone et al. (1994). For $\Omega = 1$ and $n = -2$, the power law is close to $\rho \propto r^{-2}$, consistent with flat rotation curves, but the effective power-law slope steepens significantly with increasing n and with decreasing mass. However, the density profiles have significant curvature in the $\log\rho - \log r$ plane, steepening with increasing radius. Better two-parameter fits than a power law $\rho \propto r^{-\alpha}$ to the spherically averaged density and circular velocity profiles are provided by the Hernquist (1990) or Navarro et al. (1995, 1996) analytical models, which each have a scale radius b, and thus a logarithmic slope which changes with radius. Both of these models have density profiles which are shallower than r^{-2} at $r \ll b$ and steeper at $r \gg b$. The Hernquist model changes slope too abruptly to match the simulated haloes over the full range of resolved scales, but the NFW model is an excellent fit to all our mean halo profiles. The NFW model also reproduces other dynamical properties of the simulated haloes interior to their virial radii r_{178}. Ignoring the small radial anisotropy of the halo velocity dispersion tensor, the slow variation of velocity dispersion with radius is well matched by that in the isotropic NFW model. Once the radius r_{178} has been measured for a halo, the NFW model has only one free parameter, a dimensionless scale radius $a_N = b_N/r_{178}$. It is remarkable that such a simple one-parameter function is able to fit the density profiles of haloes over a wide range of masses and initial conditions. Formally, the Hernquist and NFW models imply density varying as $\rho \propto r^{-1}$ at very small radii ($r \ll b$), but, even in our best resolved haloes, our profiles only extend down to $r/b_N \approx 0.3$, where the slope for the NFW model is approximately $r^{-1.5}$, so we have not proved that the asymptotic r^{-1} dependence is correct.

The dependence of the dimensionless scale radius, a, on halo mass and on the slope of the initial power spectrum is of particular interest. Lacey & Cole (1993, 1994) demonstrated that higher mass haloes have higher accretion rates and more recent formation epochs than their lower mass counterparts, where the formation time is defined as the time at which half the present mass of a given halo had already been assembled. Also, for a given M_{178}/M_*, the halo formation time is earlier for increasing spectral index n. If the inner regions or 'core' of the final halo formed mostly from the material that assembled earlier, then they should reflect the background density of the universe at the time they were assembled, and be denser for haloes that formed earlier. Therefore one predicts denser, more concentrated, cores for haloes with earlier formation times. This is precisely the trend we find in the simulated haloes. For fixed n, the lower mass haloes are more concentrated, with smaller values of a, while, at fixed mass, a decreases with increasing n. Navarro et al. (1996) investigate the first of these trends for the CDM model, and find a quite good proportionality between the core density and the density of the universe at the formation time.

The dependence of the density profiles and rotation curves on the spectral index is also in qualitative agreement with the results of Quinn et al. (1986), Efstathiou et al. (1988) and Crone et al. (1994), who found steeper profiles for power spectra with more small-scale power, i.e. increasing n. Crone et al. (1994) found no significant dependence of the density profiles on halo mass. However, they examined a smaller range of halo masses than in the present paper. They also applied a correction procedure intended to compensate for the effect of the finite force resolution in their simulations. This correction made all their haloes have steeper core density profiles. We tested this procedure on our haloes with similar results. However, we did not find that it improved the agreement between the halo profiles with the same M_{178}/M_* from two different output times. Thus, although the procedure alters the density profiles, it is not clear that it is usefully correcting for all the effects of limited resolution, which include not only force resolution but also finite particle number and limited range of scales in

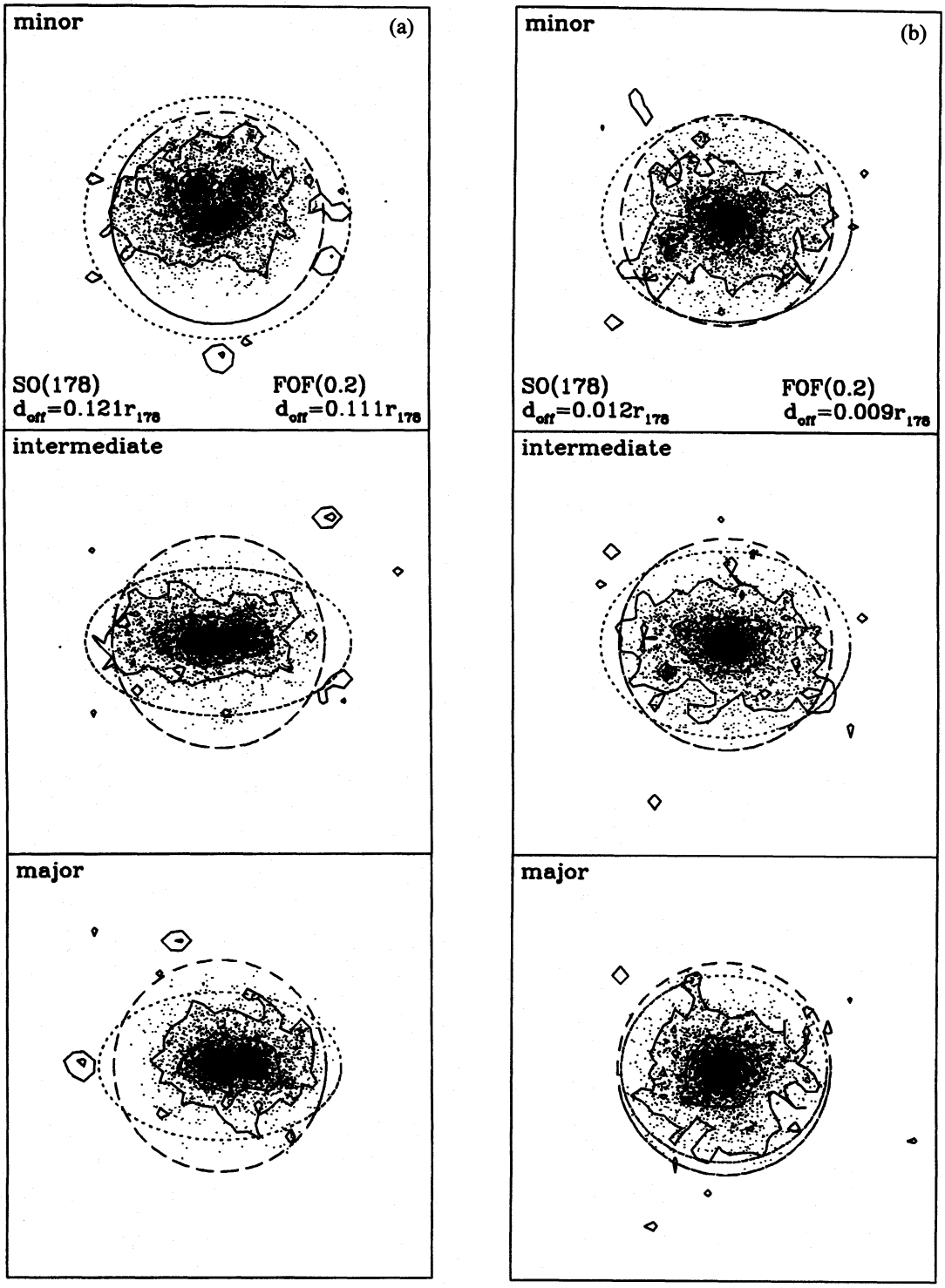

Figure 17. A selection of four groups from the $n = -1$ simulation with masses in the range $8 < M_{178}/M_* < 16$ ($3576 < N < 7152$), showing the variety of group morphologies and comparing the FOF(0.2) group definition with that of SO(178). The particles plotted are those defined as a group by the SO(178) algorithm. Each group is shown projected along the three principal axes defined by the inertia tensor of the material within the sphere of radius r_{178}. In each panel the dashed circle marks the projected boundary of this sphere. The flattening and orientation of the inertia tensor are indicated by the dotted ellipses. The contours show the projected density of all particles within $2r_{178}$. The contour levels are 0.5, 2 and 8 times the mean projected surface density within the r_{178} circle. The outer connected contour corresponds quite accurately to the boundary of the group defined by the FOF(0.2) algorithm. The values of d_{off} given in the upper panel of each figure are the offsets of the potential centre from the group centre of mass for the SO(178) and FOF(0.2) group definitions.

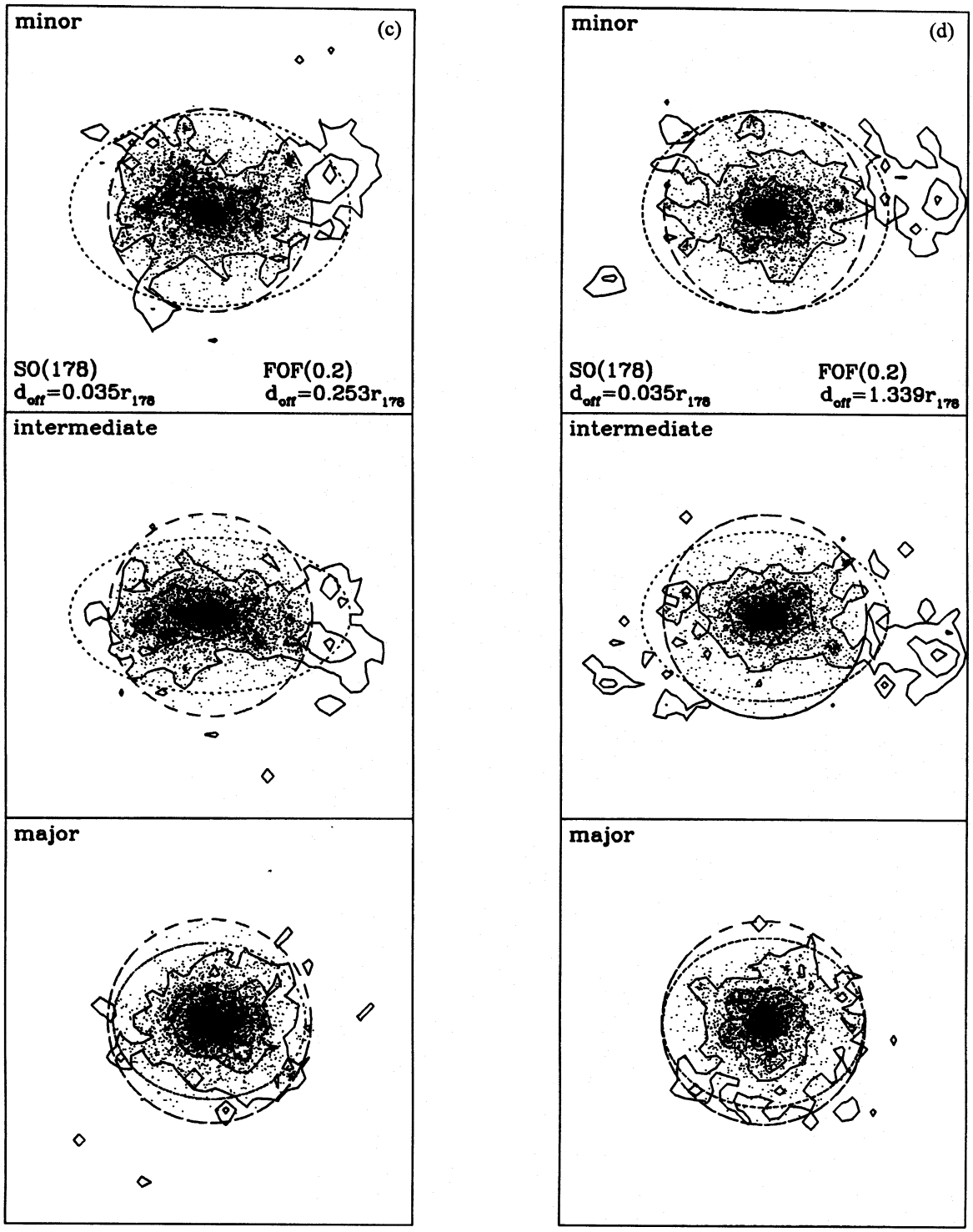

Figure 17 – *continued*

the initial conditions. Thus we preferred to leave the density profiles uncorrected and instead fitted the analytical models only over the range $\eta < r < r_{178}$, where comparison of the different output times showed the density profiles to be robust.

We can also compare our results with the analytical model of secondary infall around density peaks developed from the work of Gunn & Gott (1972) by Hoffman & Shaham (1985). Hoffman & Shaham predicted power-law halo density profiles, with logarithmic slope equal to -2 for $n \leqslant -1$ and $-(9+3n)/(4+n)$ for $n > -1$. We find that the profiles depart from power laws, though the average profile slopes are similar to the Hoffman–Shaham values over the regions where we can measure them, and Hoffman–Shaham predicts the correct trend of steeper profiles with increasing n. However, the

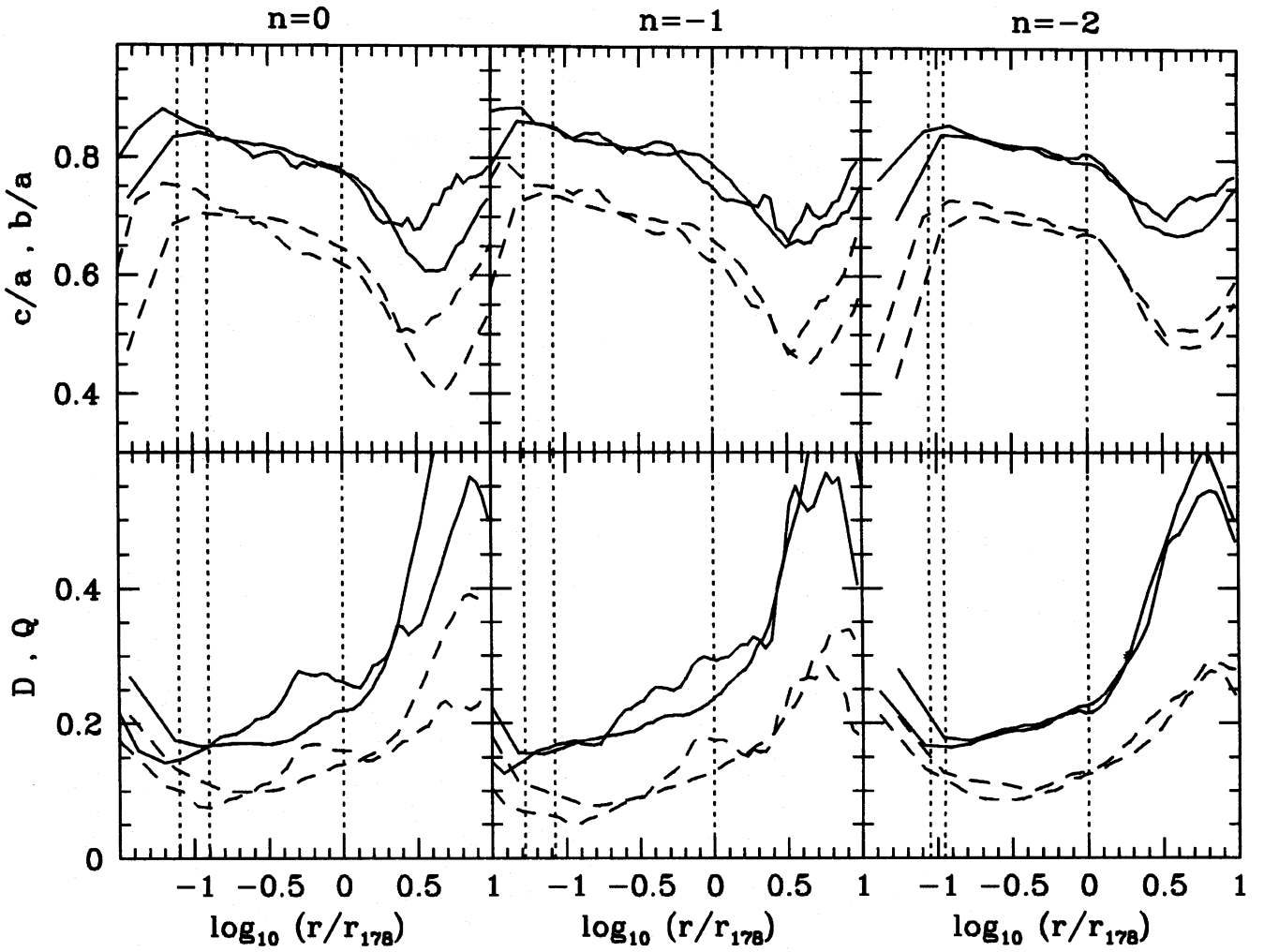

Figure 18. For each of the three simulations the curves in the upper panels show the axial ratios b/a (solid) and c/a (dashed) of the inertia tensor of material in spheres. The curves shown for $n = 0$ are for masses $1 < M_{178}/M_* < 2$ and $4 < M_{178}/M_* < 8$. For $n = -1$ curves for the two mass ranges $2 < M_{178}/M_* < 4$ and $8 < M_{178}/M_* < 16$ are shown. For $n = -2$ the mass ranges are $8 < M_{178}/M_* < 16$ and $32 < M_{178}/M_* < 64$. The curves in the lower panels show the corresponding dipole, $D(r)$ (dashed), and quadrupole, $Q(r)$ (solid), values. As before, the vertical dotted lines mark the force-softening scale η for the two mass ranges and the virial radius r_{178}. In every case, for $r_{178} < \eta$, the curve corresponding to the higher of the two mass ranges turns over at the smaller radius. This reflects the higher resolution with which more massive haloes are simulated. Note that M_* equals 266, 447 and 46.8 in the $n = 0$, -1 and -2 simulations respectively.

Hoffman–Shaham model also predicts that the profile shapes should be independent of halo mass, which disagrees with our N-body results.

We have investigated how best to draw the boundary between the region of a halo that is virialized and in approximate dynamical equlibrium, and the outer parts which are still infalling. This is particularly important if one wants to define a total virialized mass for the halo, to use in comparing with theoretical models that express results in terms of a total halo mass. An example of the latter is the Press–Schechter model for the mass function of haloes (Press & Schechter 1974), and its extension to statistics of halo mergers (Lacey & Cole 1993, 1994). Our starting point was the spherical collapse model, which, for the collapse of a uniform sphere in an $\Omega = 1$ universe, predicts that the virialized region lies interior to a radius r_{178} for which the mean density is 178 times the background value. We then find that the mean radial velocity profiles plotted in the dimensionless form V_r/V_{178} versus r/r_{178} all look very similar for different n and different M_{178}/M_*, and all show a break at $r \approx r_{178}$ from a quasi-static interior with $V_r \approx 0$ to an infalling exterior (for $1 \lesssim r/r_{178} \lesssim 4$) with $V_r < 0$. Thus, the radius r_{178} and the corresponding enclosed mass M_{178} do indeed provide good characterizations of the radius and mass of the virialized region. The shape of the mass distribution also becomes significantly more non-spherical beyond r_{178}, consistent with a break between dynamically relaxed inner regions and unrelaxed outer regions, and supporting the choice of r_{178} as the virial radius. On the other hand, the virial ratio $2T/|W|$ in spheres varies smoothly through r_{178}, and at r_{178} exceeds the value $2T/|W| = 1$ for an isolated object in dynamical equilibrium by 10–20 per cent, principally because of the confining effect of the external infalling material. Thus, the value of $2T/|W|$ does not provide a good criterion for deciding where the virialized region ends.

Crone et al. (1994) followed a similar procedure to us, but instead chose an overdensity of 300 to define the edge of

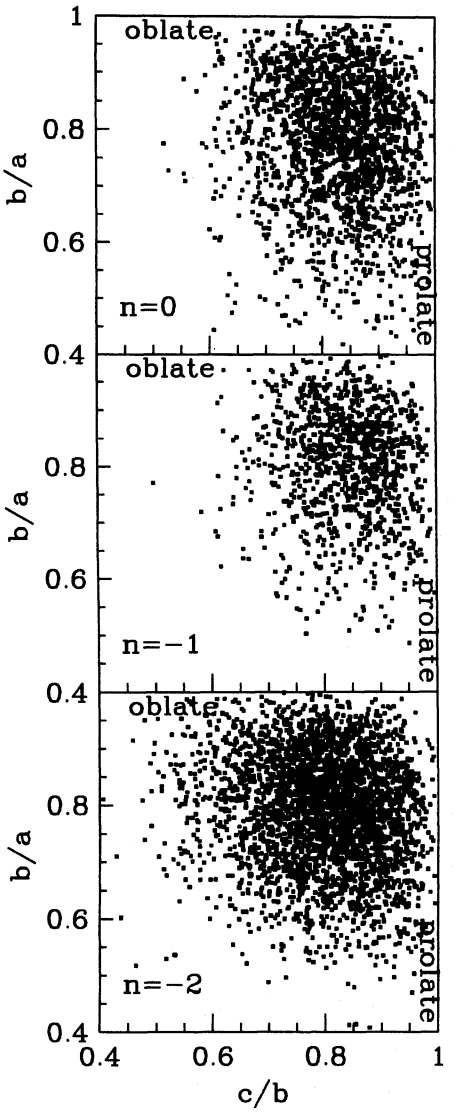

Figure 19. The distribution of the axial ratios b/a and c/b for the inertia tensor of the mass interior to r_{178} for SO(178) groups with masses $M_{178} \geqslant M_*$ from each of the three simulations. The loci of prolate ($c/b = 1$) and oblate ($b/a = 1$) shapes are indicated.

the virialized region. In practical terms, the difference from our choice is not that large. For the haloes in our simulations, the dimensionless scale radius spans the range $0.05 \lesssim a_N \lesssim 0.3$. For this range, the NFW model gives $r_{300}/r_{178} \approx 0.8$ and $M_{300}/M_{178} \approx 0.8 - 0.9$, where r_{300} and M_{300} are defined analogously to r_{178} and M_{178}.

The halo properties we analysed are largely independent of the algorithm used to identify the groups, for the SO method with mean overdensity in the range $\kappa = 100 - 400$, and for the FOF method with linking length in the range $b = 0.15 - 0.3$, corresponding to a local overdensity in the range $20 - 140$. The halo profiles are insensitive to exactly which particles are identified as group members because we use the minimum in the gravitational potential to define the halo centre, and include all the surrounding material when constructing the halo profiles.

What group-finder partitions the particle distribution into objects that best correspond to virialized haloes according to the results above? Not surprisingly, the raw groups found by the SO(178) algorithm mostly match very well with the material interior to r_{178} around the halo centre, defined as the minimum in the gravitational potential. The difference is that the raw SO(178) groups are defined so that the centre of mass of the group coincides with the centre of the sphere. The FOF(0.2) groups mostly also match fairly well to the material within r_{178} of the halo centre, as defined above, but occasionally the FOF(0.2) algorithm links two distinct haloes that are soon to merge, and in such cases the offset between the FOF(0.2) group centre of mass and the potential centre can be large. The masses of the FOF(0.2) groups mostly agree well with the virial masses M_{178}, with a spread around this of only about 20 per cent, but with larger deviations for haloes in the process of merging. This provides some post hoc justification for the extensive use of the FOF(0.2) algorithm in computing halo properties and mass functions.

9 CONCLUSIONS

We have studied the structure of haloes that are formed in simulations of self-similar clustering models with $n = 0, -1, -2$ and $\Omega = 1$, over a wide range in halo mass.

(1) We find that the radius r_{178} about the halo centre within which the mean overdensity is 178 accurately demarcates the virialized interior of the halo, which is in approximate dynamical equlibrium, from the exterior, where material is still falling in. The characterization of r_{178} as the 'virial radius' agrees with the prediction of the simple spherical collapse model.

(2) For $r < r_{178}$, the spherically averaged density, circular velocity and velocity dispersion profiles are very well fitted by the analytical model of Navarro et al. (1995, 1996) with an isotropic velocity dispersion. This model has $\rho \propto r^{-1}$ at $r/r_{178} \ll a_N$, rolling over to $\rho \propto r^{-3}$ at $r/r_{178} \gg a_N$, where a_N is a dimensionless scale radius. It should be noted that even for our best resolved haloes the NFW model has $\rho \propto r^{-1.5}$ at the softening radius, and thus we do not probe the asymptotic prediction of $\rho \propto r^{-1}$.

(3) The value of the dimensionless scale radius a_N correlates strongly with halo mass and with spectral index n. Haloes with mass M much less than the characteristic mass M_* typically form much earlier than haloes with $M \gg M_*$. This results in them being more centrally concentrated (smaller a_N), with cores whose densities reflect the higher mean density of the universe at their formation time. For a given M/M_*, haloes form earlier in models with more small-scale power (larger n), and also have denser cores.

Despite the successes of the spherically symmetric model, haloes are not spherical. In these $\Omega = 1$ simulations most haloes show evidence of substructure and many are clearly about to undergo a merger.

(4) Haloes are generically triaxial, but with a slight preference for prolate configurations, at least for $n = -1$ and 0. Their inertia tensors (measured in spheres) have typical axial ratios $1 : 0.8 : 0.65$ at the virial radius r_{178}, becoming gradually more spherical towards their centres. There is no significant trend with mass or spectral index. Measurements of the dipole moments of the mass distribution around halo centres show them to have mean dipoles of order 10 per cent, and similarly large quadrupole distortions.

(5) Haloes are slowly rotating, with $V_{\rm rot}/\sigma \approx 0.3$. The rotation velocity $V_{\rm rot}$ measured in spherical shells is approximately constant with radius, but the angular momentum is not well aligned between the central and outer regions. The median value of the spin parameter (measured interior to r_{178}) is $\lambda \approx 0.04$ with a weak trend for lower λ at higher halo mass. There is no significant trend of λ with spectral index.

(6) The properties we find are insensitive to the details of the group-finding algorithm used to select the haloes in the simulations, since, once we have identified a group, we define the halo centre from the minimum of the potential, and include all surrounding particles when computing profiles.

The simple analytical description in (1)–(3) of the spherically averaged profiles of dark matter haloes has many applications. It will enable refined modelling of galaxy formation and dynamics, and improved calculations of gravitational lensing properties. A similarly detailed analysis of haloes formed in open models and models with a cosmological constant will be extremely interesting, and may lead to new diagnostics in which the halo density profiles can be used to discriminate between different cosmological models.

ACKNOWLEDGMENTS

We thank George Efstathiou for supplying us with a copy of his P^{3}M N-body code. SMC gratefully acknowledges the support of a PPARC Advanced Fellowship. CGL was supported by a PPARC Advanced Fellowship at Oxford, and by the Danmarks Grundforskningsfond through its support for the establishment of the Theoretical Astrophysics Center.

REFERENCES

Barnes J., Efstathiou G. P. E., 1987, ApJ, 319, 575
Cole S., Aragon-Salamanca A., Frenk C. S., Navarro J. F., Zepf S., 1994, MNRAS, 271, 781
Crone M. M., Evrard A. E., Richstone D. O., 1994, ApJ, 434, 404
Davis M., Efstathiou G., Frenk C. S., White S. D. M., 1985, ApJ, 292, 371
Dubinski J., Carlberg R., 1991, ApJ, 378, 496
Efstathiou G., Davis M., Frenk C. S., White S. D. M., 1985, ApJS, 57, 241
Efstathiou G., Frenk C. S., White S. D. M., Davis M., 1988, MNRAS, 235, 715
Frenk C. S., White S. D. M., Efstathiou G., Davis M., 1985, Nat, 317, 595
Frenk C. S., White S. D. M., Davis M., Efstathiou G., 1988, ApJ, 327, 507
Gunn J. E., Gott J. R., 1972, ApJ, 176, 1
Hernquist L., 1990, ApJ, 356, 359
Hoffman Y., Shaham J., 1985, ApJ, 297, 16
Kauffmann G., White S. D. M., Guiderdoni B., 1993, MNRAS, 264, 201
Lacey C. G., Cole S., 1993, MNRAS, 262, 627
Lacey C. G., Cole S., 1994, MNRAS, 271, 676
Narayan R., White S. D. M., 1988, MNRAS, 231, 97P
Navarro J. F., Frenk C. S., White S. D. M., 1995, MNRAS, 275, 720 (NFW)
Navarro J. F., Frenk C. S., White S. D. M., 1996, ApJ, 462, 563
Press W. H., Schechter P., 1974, ApJ, 187, 425
Quinn P. J., Salmon J. K., Zurek W. H., 1986, Nat, 322, 329
Warren M. S., Quinn P. J., Salmon J. K., Zurek W. H., 1992, ApJ, 399, 405
Zurek W. H., Quinn P. J., Salmon J. K., 1988, ApJ, 330, 519

This paper has been produced using the Royal Astronomical Society/Blackwell Science LaTeX style file.